Bolted steel to laminated timber and glubam connections

DOI:
10.1016/j.ijmecsci.2023.108364

Document Version
Accepted author manuscript

Citation for published version (APA):
Shi, D., Huang, H., Li, N., Liu, Y., & Demartino, C. (2023). Bolted steel to laminated timber and glubam connections: Axial behavior and finite-element modeling. *International Journal of Mechanical Sciences*, *252*, [108364]. https://doi.org/10.1016/j.ijmecsci.2023.108364

Published in:
International Journal of Mechanical Sciences

Graphic abstract

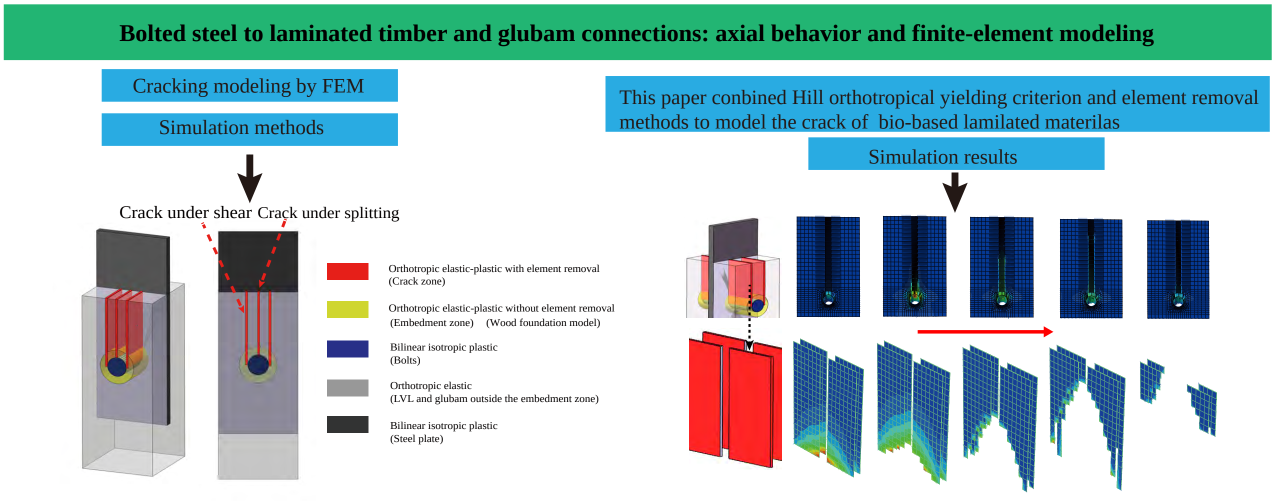

Highlights

Bolted steel to laminated timber and glubam connections: axial behavior and finite-element modeling

Da Shi, Haonan Huang, Ning Li, Yiwei Liu, Cristoforo Demartino

- LVL connections exhibit higher ductility and lower capacity compared to glubam.
- High-fidelity finite-element model integrating Hill's yielding and element removal criteria.
- The proposed element removal criterion can effectively simulate crack growth.
- The Hill yielding criteria in UMAT subroutine can effectively model plastic behavior.
- The proposed theoretical formula can effectively predict the initial stiffness.

Bolted steel to laminated timber and glubam connections: axial behavior and finite-element modeling

Da Shi[a,d], Haonan Huang[a], Ning Li[b], Yiwei Liu[c], Cristoforo Demartino[d,e,*]

[a] *College of Civil Engineering and Architecture, Zhejiang University, 866 Yuhangtang Road, Hangzhou, 310058 Zhejiang, China*
[b] *Department of mechanical, Aerospace and Civil Engineering, University of Manchester, M13 9PL, United Kingdom*
[c] *Key Laboratory for Green and Advanced Civil Engineering Materials and Application Technology of Hunan Province, College of Civil Engineering, Hunan University, 410082, China*
[d] *Zhejiang University - University of Illinois at Urbana Champaign Institute, Zhejiang University, Haining 314400, Zhejiang, PR China*
[e] *Department of Civil and Environmental Engineering, University of Illinois at Urbana-Champaign, Urbana, IL 61801, USA*

Abstract

This study aims to characterize the axial monotonic and cyclic tensile behavior of bolted steel connections to laminated timber and bamboo, using slotted-in steel plates, and to provide a high-fidelity simulation using finite-element modelling. Forty-eight experimental tests were conducted, including eight different configurations, varying in material (Laminated Veneer Lumber (LVL) and Glued Laminated Bamboo (glubam)), number of bolts, and diameter of bolts, under tension, both monotonic and cyclic (three repetitions). The force and displacement were recorded, and used to define the initial stiffness, yielding strength, ultimate strength, ductility, viscous damping, and energy dissipation. The failure modes of the connections were monitored using Digital Image Correlation (DIC) techniques. A novel high-fidelity finite-element model integrating Hill's yielding and element removal criteria was proposed to predict the mechanical performance and fracture behavior of the examined connections. The numerical simulation was validated by comparing the experimental load-displacement curves and the strain field measurements obtained with DIC. Finally, theoretical formulas for predicting the stiffness of bolted connections were proposed based on the FEM simulations.

Keywords: Bolted connections, Glue laminated materials, Composite wood, LVL, glubam, FEM

Contents

*Corresponding author
Email addresses: da.21@intl.zju.edu.cn (Da Shi), huanghn@zju.edu.cn (Haonan Huang), ning.li-3@manchester.ac.uk (Ning Li), yiweiliu@hnu.edu.cn (Yiwei Liu), cristoforodemartino@intl.zju.edu.cn (Cristoforo Demartino)

1. Introduction

The construction industry widely employs bio-based laminated composite materials made from timber and bamboo due to their favorable properties, including mechanical strength, renewable nature, economic viability, and carbon storage capacity [1, 2]. To manufacture such materials, the lamination process is used, which involves joining multiple layers of natural bamboo and timber using adhesives. This results in engineered structural materials that have enhanced properties and are free from the irregularities of the parent natural materials. The mainstream engineered timber products used in the industry include structural composite lumber (SCL), glued-laminated timber (GLT), cross-laminated timber (CLT), and nailed-laminated timber (NCL) [3, 4]. In contrast, the most commonly used engineered bamboo products are laminated bamboo [5], bamboo scrimber [6, 7], and bamboo woven panel [8]. In this context, two different bio-based laminated materials, Laminated Veneer Lumber (LVL) [9, 10] and glued laminated bamboo (glubam) [11, 12, 13], are typically used as the primary component of bolted joints.

Wood joints have evolved significantly over time, with various types such as tenon-mortise, tooth, bolted, metal-plate, and planting bar connections being developed to optimize their performance [14]. Bolted connections with slotted-in steel plates are among the most commonly used types in wooden truss and moment resisting frame structures. Research has been conducted over many years to analyze the mechanical behaviors of these connections. For instance, Platt and Harries [15] used an experimental program to investigate the bolted lap-splice behaviors of the bolted laminated bamboo connections in an aim to explore potential applications of using laminated bamboo strips to repair timber structures. He et al. [16], Lam et al. [17], Shu et al. [18], Wang et al. [19] used the bolted glulam connections with slotted-in steel plate as knee braces for glulam beam-to-column connections and investigated its moment resisting performance. Leng et al. [20] studied the moment-rotation behavior of beam-to-column bolted connections in bamboo scrimber structures. Three types of beam-to-column connections were designed and the influence of bolt arrangement and the local inclusion of cross-laminated laminae locally in the connection region were investigated [21]. These studies indicates that the specimens having cross-laminated laminae can avoid parallel-to-grain splitting failure initiating at the bolt lines. Stehn and Börjes [22] investigated the influence of ductile connections, slotted-in nailed wood to steel joints, on the total load-carrying capacity and deformability of a glulam truss. Kobel et al. [23] experimentally investigated the application of LVL made of European beech wood in timber truss structures showing that dowel-type connections can ensure high load-carrying capacities and ductile behavior. Innovative moment-resisting connections for mid-rise timber moment frame structural systems have been proposed by Shu et al. [24]. These connections are reinforced by long steel rods with screwheads and long self-tapping screws, providing a stiff and resilient beam-to-column connection. The proposed system eliminates the need for shear walls or braces. Wu and Xiao [25] proposed a new type of hybrid space truss system composed of steel lower chord and glubam upper chords and web elements. The specially designed steel glubam hybrid space truss system was successfully designed and constructed for a rain-shed canopy of an office building.

The Finite Element Model (FEM) of these connections requires an accurate definition of material constitutive [26]. Hill yield criterion was commonly used in the numerical model of wood due to its orthotropic characteristics [27, 28, 29]. Although the softening behavior of LVL and glubam was simulated to some extent by Hill yield criterion, no crack propagation was considered in this criterion. Elasto-plastic material in compression with Hill yield criterion and linear elastic material in tension with the maximum stress failure criterion were used in the numerical model of Kharouf et al. [30]. A three-dimensional elasto-plastic model considering the material degradation was developed by Wang et al. [31]. To better describe the local crushing behavior of the wood near the bolts in connections, a wood foundation model was proposed by Hong and Barrett [32]. The material properties of the wood near the bolts were obtained by embedment tests. Cohesive zone material laws were used by He et al. [16] to trace the crack propagation of glulam connections.

However, an high-fidelity FE model of the axial monotonic and cyclic tensile behavior of bolted steel to laminated timber and bamboo connections, using slotted-in steel plates has not been investigated and is still not available.

In this framework, this study experimentally investigates the axial monotonic and cyclic tensile behavior of bolted steel to laminated timber (LVL) and bamboo (glubam) connections, using slotted-in steel plates, and provides a high-fidelity simulation using finite-element modeling. Results of the material property are presented and discussed in Section 2.1. Section 2.2.1 provides detailed information on the specimens and their fabrication process. Forty-eight experimental tests were conducted, including eight different configurations that varied by material (Laminated Veneer Lumber (LVL) and Glued Laminated Bamboo (glubam)), bolt number, and diameter. Each configuration was repeated three times under monotonic and cyclic loading, respectively. The test set-up and loading regime are introduced in Sections 2.2.2. The experimental results (monotonic and cyclic) are summarized in Section 2.3. Based on the experimental findings, this study provides an innovative finite-element model for high-fidelity simulations (Section 3). In particular, this study attempts to simulate the cracking behavior by combining Hill yield criterion with other failure criteria [33, 34]. The proposed model implements the element removal criterion in the observed cracking area that can be determined through experimental observations. On the basis of previous researches [35], Section 4 provides the derivation of theoretical formulas for the initial stiffness of double bolted connections calibrated based on the outcomes of the FEM simulations. Finally, conclusions and perspectives are drawn in Section 5.

2. Experimental tests

This Section describes the experimental test adopted to validate the proposed FE model and reports the results. Section 2.1 describes the tests performed on the LVL and glubam together with the found material properties. Section 2.2 reports the experimental tests performed providing an extensive description of the specimens and test set-up. Finally, Section 2.3 provides results of the monotonic and cyclic tests. The failure modes are also discussed.

2.1. Materials testing

The materials adopted in this study are: LVL, glubam, high-strength bolts (grade 8.8) with a length of 120 mm and a diameter of 8 and 10 mm, washers with external diameters of 14 and 16 mm for bolts of 8 and 10 mm, respectively, and Q235 steel plate with a thickness of 8 mm. LVL is an engineered timber composite manufactured by laminated wood veneers with a thickness of $2-4$ mm using exterior-type adhesives [36]. LVL is made of poplar. Glubam is a type of engineered bamboo composite that resembles timber-based glued-laminated lumber [37, 38]. Glubam is composed of Moso Bamboo strips that undergo cleaning and drying processes to reach a moisture content of 18%. Subsequently, the strips are saturated in phenol formaldehyde resin.

Material tests were carried out to determine parallel-to-the-grain compression strength ($f_{c,0}$), elastic modulus (E_0), parallel-to-the-grain shear strength ($f_{v,90}$), perpendicular-to-the-grain tensile strength ($f_{t,90}$), dowel bearing strength or embedment strength ($f_{h,0}$) and stiffness ($k_{h,0}$), and density (ρ). The subscript 0 indicates parallel-to-the-grain direction while 90 refers to perpendicular-to-the-grain direction. Figure 1 [39] summarizes the specimen geometry and test setup adopted to define the material properties previously discussed. All the tests were repeated six times.

$f_{c,0}$ and E_0 were determined according to GB/T 50329-2002 [40]. $f_{v,0}$ is determined according to ASTM D143 [41] with specimens having geometry reported in Figure 1b. $f_{v,0}$ is the peak load measured on the testing machine divided by the applied area (50×50 mm, see Figure 1b). $f_{t,90}$ is determined according to ASTM D143 [41] with specimens having geometry reported in Figure 1c. $f_{h,0}$ was measured according to ASTM D 5764-97a [42] using four specimens for each material having geometry reported in Figure 1d. A 8- and 10-mm-diameter smooth tungsten steel dowel was employed in the tests. $k_{h,0}$ is the elastic stiffness calculated in the $10-40\%$ of peak load range as the stress divided by the corresponding displacement.

Table 1 presents the average test results and coefficient of variations (CV) of LVL and glubam. E_0 is larger for LVL and $f_{c,0}$ for glubam. Similar results were reported in the literature for LVL [43, 44, 45] and for glubam [46, 38]. $f_{v,0}$ and $f_{t,90}$ are slightly larger for glubam and consistent with those reported in the literature [25, 38, 47]. $f_{h,0}$ and $k_{h,0}$ are calculated from the stress-displacement curves of dowel bearing strength tests. $f_{h,0}$ and $k_{h,0}$ is larger for glubam and similar results were reported in the literature for LVL [48, 49] and for glubam [46, 50, 38]. It is noteworthy that $k_{h,0}$ is expressed in the form of stress divided by the displacement, therefore $k_{h,0}$ should be multiplied by d to obtain the stiffness per unit length in Winkler model [51].

The bolts were tested to determine the bending yield moment (M_y) and nominal yield strength (f_{yb}) according to ASTM F1575-2003 [52]. The average M_y and f_{yb} are 62 N $\cdot$ m and 721 MPa for 8 mm bolt and 137 N $\cdot$ m and 824 MPa for 10 mm bolt.

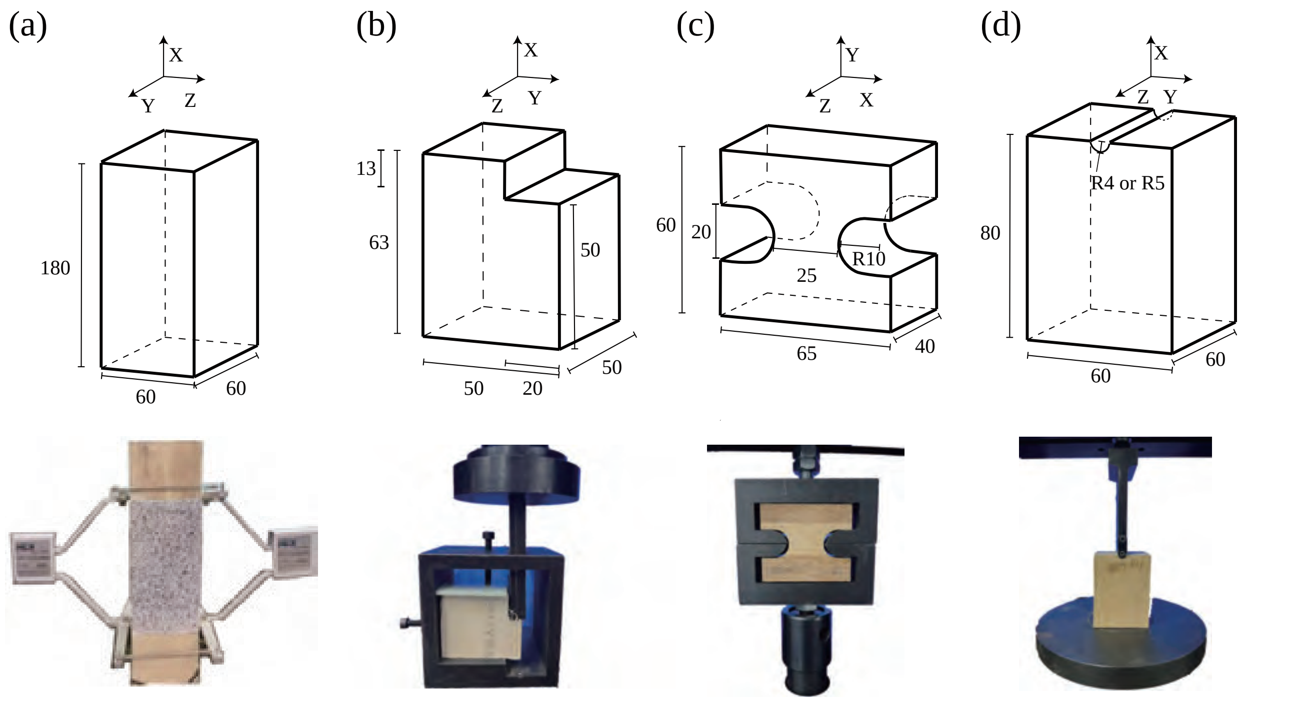

Figure 1: Specimen geometry and test setup for measuring compression strength and elastic modulus (a), parallel-to-the-grain shear strength (b), perpendicular-to-the-grain tension strength (c) and dowel bearing strength (d). Adapted from [39].

Table 1: Properties of LVL and glubam. The number in the parenthesis indicates the Coefficient of Variation (CV). After [39].

Material	E_0 [GPa]	$f_{c,0}$ [MPa]	$f_{v,0}$ [MPa]	$f_{t,90}$ [MPa]	$f_{h,0}$ (8 mm) [MPa]	$f_{h,0}$ (10 mm) [MPa]	$k_{h,0}$ (8 mm) [MPa/mm]	$k_{h,0}$ (10 mm) [MPa/mm]	ρ [kg/m^3]
LVL	11.45 (13%)	38 (6%)	6.98 (7%)	1.81 (25%)	40 (3%)	37 (8%)	42 (4%)	45 (10%)	614 (7%)
Glubam	8.56 (8%)	62 (13%)	8.18 (11%)	2.69 (14%)	86 (4%)	81 (7%)	79 (4%)	61 (6%)	749 (5%)

2.2. Experimental tests

2.2.1. Specimens: design and fabrication

The specimens were purposely fabricated to be affixed to the clamps of the testing machine, see Figure 3. To prevent any local damage or significant deformation of the LVL or glulam block, steel plates were consistently used to connect the specimens to the two clamps. Consequently, the specimens are equipped with two dissimilar slotted-in steel plates at either end (refer to Figure 2). The tested side, where connection damage is anticipated to occur (left side in each subfigure of Figure 2), is connected with fewer bolts. The other side is intended to have an adequately high capacity to endure the tests without damage. Hence, a larger number of bolts (four) is always utilized. The length of the connection specimen was established to strike a balance between the two conflicting requirements of having a sufficient length to evade interaction between the two connections at either end and the limited space available in the testing apparatus (refer to Section 3).

Four different configurations were investigated in this study, namely single and double bolts ($n = 1$ or 2) and with a diameter of $d = 8$ and 10 mm. Moreover, LVL and glubam members are considered leading to a total of eight different configurations. Connections on the tested side are designed following geometric requirements of GB50005 [53]. The specimen configurations for single bolt and double bolts are summarized in Figure 2. The same geometry was considered for LVL and glubam and for $d = 8$ and 10 mm. Three identical specimens are tested to ensure the repeatability of the results under tensile axial monotonic and cyclic loading conditions. The geometric information of all specimens is displayed in Table 2. Specimens were named following the designation L (G)-M (C)-S (D)-X-Y. L (G) indicates materials (LVL or glubam), M (C) indicates the loading regime (Monotonic or Cyclic), S (D) is used to designate the amount of bolt used on the upper part (Single or Double), X indicates the bolt diameter (8 mm or 10 mm), Y indicates specimen number (1, 2 or 3). Therefore, a total of 48 specimens are realized. The three specimens adopted for test repetitions are fabricated using the same original blocks having a length of 4 m to ensure similar characteristics of the material employed.

The LVL and glubam member are 550 mm long and have the cross sectional dimensions of 60×60 mm and both of them are fabricated from the same batch of block with cross sectional dimensions of 60×60 mm. In all the cases, two 8 mm-wide slots are considered in the members for inserting steel plates. Holes are drilled on the LVL, glubam components and steel plates. Bolts protruding from these holes are adopted to connect the steel plate with LVL and glubam components. The steel plates were manufactured by laser cutting of Q235 steel plate and by drilling holes at specific locations. The steel plates are rectangular with a base equal to 60 mm

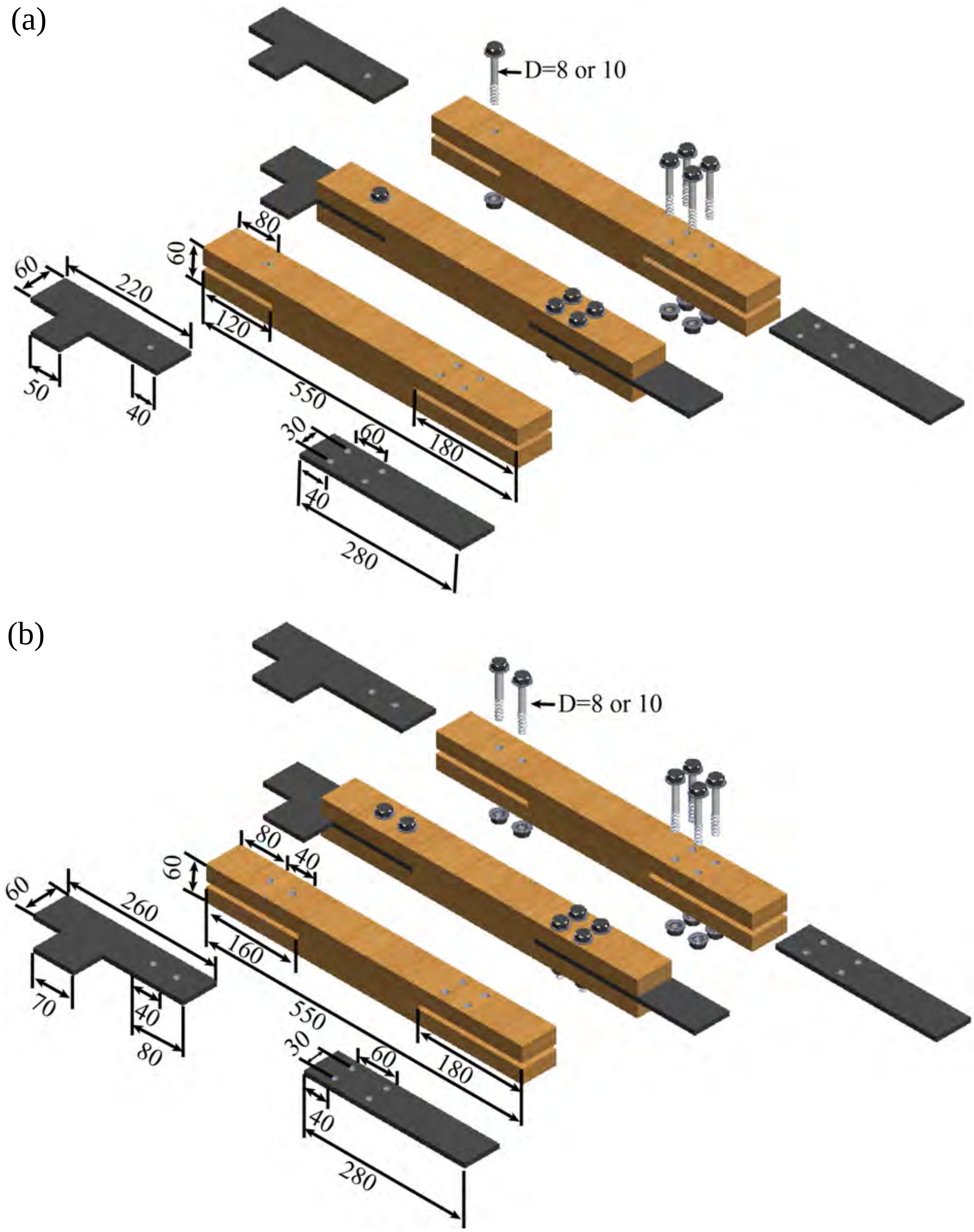

Figure 2: Configurations of single-bolted specimen (a) and double-bolted specimen (b). For each case, different diameters of bolts (8 mm or 10 mm) are considered. The specimens have two dissimilar slotted-in steel plates at each end. The tested side, where connection damage is expected, has fewer bolts. The other side has a higher capacity and always uses four bolts. The connection length is balanced between avoiding interaction between the two end connections and the limited space in the testing apparatus.

Table 2: Geometric information of different configurations. The table lists various configurations indicating the bolt diameter, bolt number, loading regime, and material used. The configurations include LVL and glulam materials, with monotonic or cyclic loading and different bolt diameters and numbers.

Configuration	Bolt diameter (mm)	Bolt number	Loading regime	Material
L-M-S-8	8	1	Monotonic	LVL
L-M-S-10	10			
L-M-D-8	8	2		
L-M-D-10	10			
L-C-S-8	8	1	Cyclic	
L-C-S-10	10			
L-C-D-8	8	2		
L-C-D-10	10			
G-M-S-8	8	1	Monotonic	Glubam
G-M-S-10	10			
G-M-D-8	8	2		
G-M-D-10	10			
G-C-S-8	8	1	Cyclic	
G-C-S-10	10			
G-C-D-8	8	2		
G-C-D-10	10			

and variable length (Figure 2). In particular, the length is equal to the sum of the slot length and 100 mm which is the zone of the plate adopted for clamping to the test machine. The steel plates on the tested side have an additional flag (rectangular area) used to connect a displacement transducer (Figure 3(c)). To ensure adequate tolerances during specimen assembly, the holes in LVL and glulam blocks were designed to be 0.5 mm larger. Torque control was a critical aspect, with high-strength bolts being tightened using a calibrated torque wrench. The torque was carefully controlled to prevent significant local deformation around washers, such as the penetration of the washer into the LVL or glulam block surface. Preliminary tests showed a pre-load torque of 0.7 N·m and 1 N·m for 8 mm and 10 mm diameter bolts, respectively, providing controlled friction conditions at the interface between the steel plate and slot surfaces.

The surfaces of the specimen opposite to the tested side, where bolt head and nuts are located, were treated for performing Digital Image Correlation (DIC) measurements, as described in Section 2.2.2. Specifically, the upper part of the specimen, located 230 mm from the end, was modified to create a high contrast texturing effect using white paint with a black speckle pattern, as depicted in Figures 3 (d).

2.2.2. Test set-up and measurements

Figure 3 illustrates the test setup used for the bolted connections. A 100 kN hydraulic actuator (186E, WANCE Ltd.) is used for the load application. The force is recorded by the actuator and the displacements at the connection through one displacement transducer. The upper end of the displacement transducer is fixed on the upper steel plate and the bottom end is fixed on the middle part of LVL and glubam elements.

Before testing, the surface of the specimens was painted with a high-contrast texturing effect, using white paint with a black speckle pattern, as shown in Figure 3(d), to carry out a strain field analysis over the surface of the specimens by DIC setup. Figure 3 provides a view of the DIC test setup. The photos were taken at a frame rate of 2/s with two cameras (body and a 25 mm lens), positioned symmetrically in front of two speckle surface, with the lens direct towards the centre of the speckle area and in perpendicular position in respect to the specimen surface. A speckle field with a size of 60mm×230mm was monitored. Two light sources of constant luminosity were used to maintain consistency in the measurements.

The software GOM Correlate was used to carry out the DIC analyses. GOM Correlate gives the displacement/strain field at each loading step by defining square-shaped sub-zones, called "facets", in the initial image and tracking these sub-zones in subsequent images. The facets were defined over the random speckle pattern sprayed on the sample surface, which facilitated the definition of a grey level distribution sufficient to differentiate the sub-zones. A facet size of 19 pixels and a spacing of 16 pixels (point distance) (for full field analysis) were defined to accommodate both a good resolution and computational viability. A standard analysis, as defined by the software, was carried out.

Tensile monotonic and cyclic tests were performed according to EN12512 [54]. The monotonic loading protocol is comprised of a preloading phase and a normal loading phase. In the first phase, the specimen was loaded up to 10% of the ultimate load (estimated using some preliminary tests) followed by a constant load for 120 s. Then, the load was decreased to zero followed by a pause of 30 s. Subsequently, the loading was

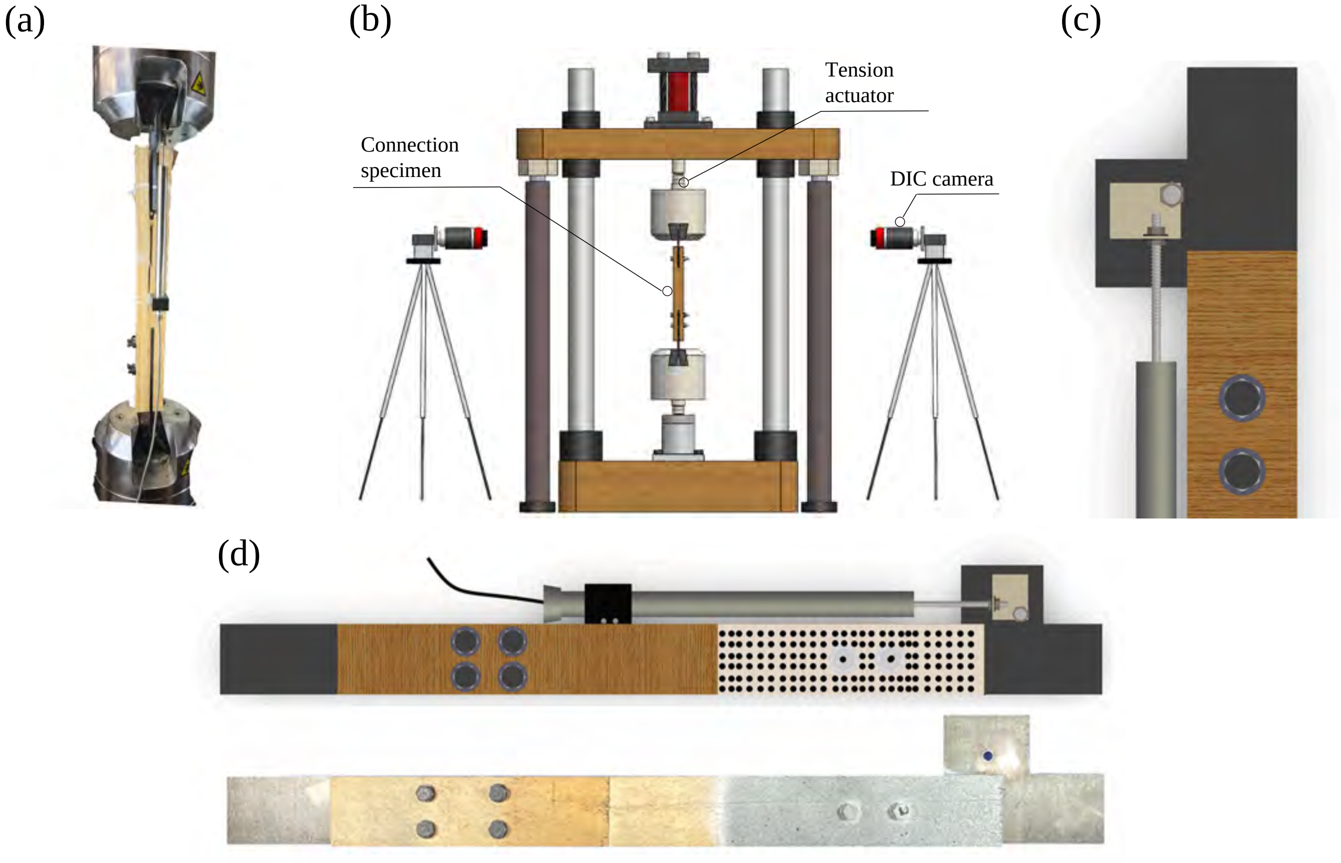

Figure 3: Test setup and instrumentation: photo (a), sketch (b), detail of the LVDT and steel flag (c,d), and speckle pattern for DIC analyses (d).

monotonically increased at a loading rate of 1.5 mm/min. The test was stopped at a displacement of 40 mm. The reason for the preloading phase was to eliminate the internal friction between the LVL, glubam component and steel plate and the settlement of the connection [55]. The cyclic loading protocol was conducted according to EN12512 [54]. However, a non-reversed modification of the procedure outlined in EN 12512 [54] was used to perform the cyclic test. The displacement was cycled from zero to a positive (tension) value without excursions into negative (compression) values [56], as shown in Figure A.23(a). The V_y varied among the configurations, depending on experimental yield values obtained from the monotonic tests in agreement with EN 26891 [57]. The cyclic loading was conducted under displacement control mode at a loading rate of 0.2 mm/s until a slip of 30 mm was reached.

Load vs. displacement curves were processed to obtain some synthetic indicators according to ASTM D5764-97a [42]. The following indicators are considered (Figure A.23(b)): initial stiffness (k_e), yielding load (F_y), maximum load (F_u), and ductility (D).

The specimens performance under cyclic loading conditions are also characterized in terms of the equivalent viscous damping (V_{eq}) and energy dissipation [58, 59, 60]. The equivalent viscous damping V_{eq}, defined as a ratio of the dissipated energy E_d to the available potential energy E_p (see Figure 4) multiplied by 2π (i.e., $V_{eq} = E_d/2\pi E_p$) can be used for evaluating the cyclic performance of the bolted connections in terms of their energy dissipation capacity.

2.3. Results

2.3.1. Monotonic loading

Load vs. displacement curves of tensile monotonic tests are shown in Figure 5. Results are reported as each of the three tests (gray lines) and average across displacements (continuous red lines). Moreover, k_e, F_y, F_u, and D (see Section 2.2.2 for their definition) of the tests reported in Figure 5 are summarized in Table B.7.

Figure 5 demonstrates the reproducibility of results for the three repetitions. The LVL and glubam connections exhibit similar trends in the elastic stage, but display different behaviors leading to various loading plateaus and failure modes. The load-displacement curves of glubam specimens exhibit a shorter load plateau stage and experience an abrupt failure due to longer propagating cracks. Conversely, the load-displacement curves of LVL connections are smoother, displaying a longer-lasting loading plateau stage. This distinction can

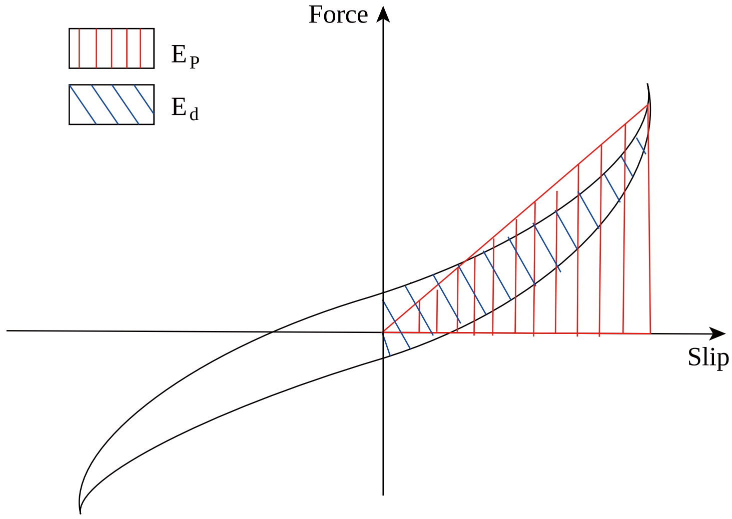

Figure 4: Determination of equivalent viscous damping on the hysteretic curve (force vs. displacement). The black line is the histeretic curve for one cycle. The blue shaded area corresponds to the dissipated energy E_d and the red shaded area corresponds to the available potential energy E_p.

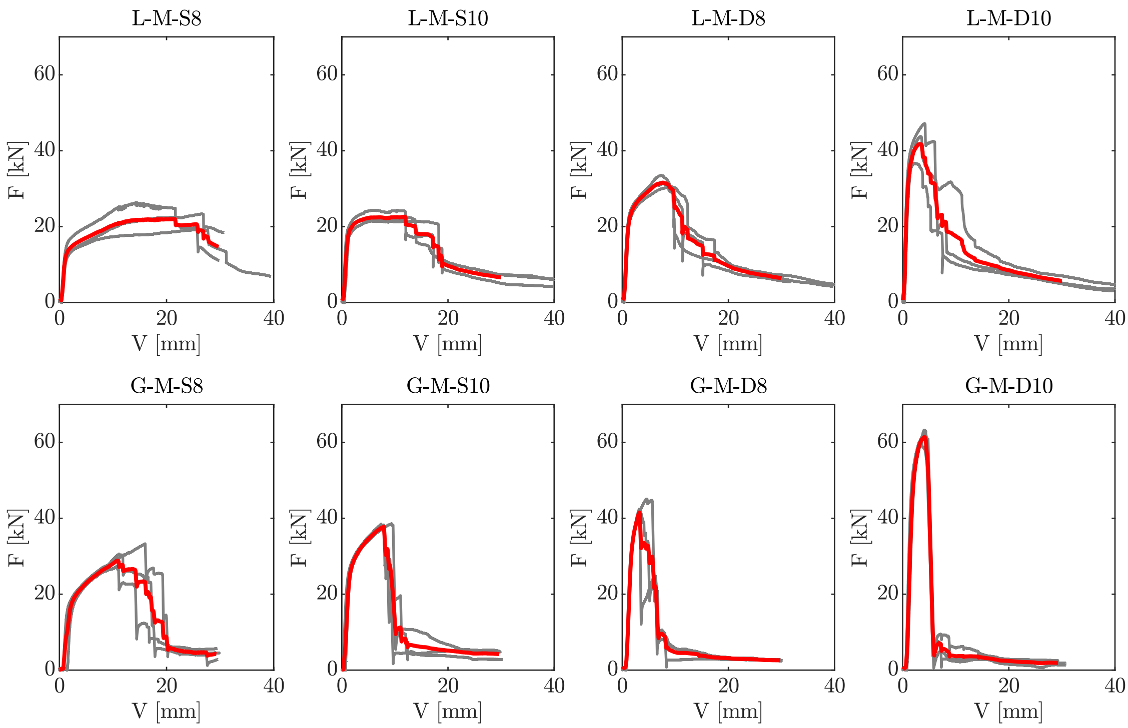

Figure 5: Load (F in kN) vs. displacement (V in mm) curves of tensile monotonic tests. The first row refers to tests performed on LVL while the second refers to glubam. The first two columns refers to single bolt and the last two to double bolts cases. The three gray lines are the three tests repetitions. The red line is the average of three tests across displacements. The averare line ends when one of the test data is not available. After [39].

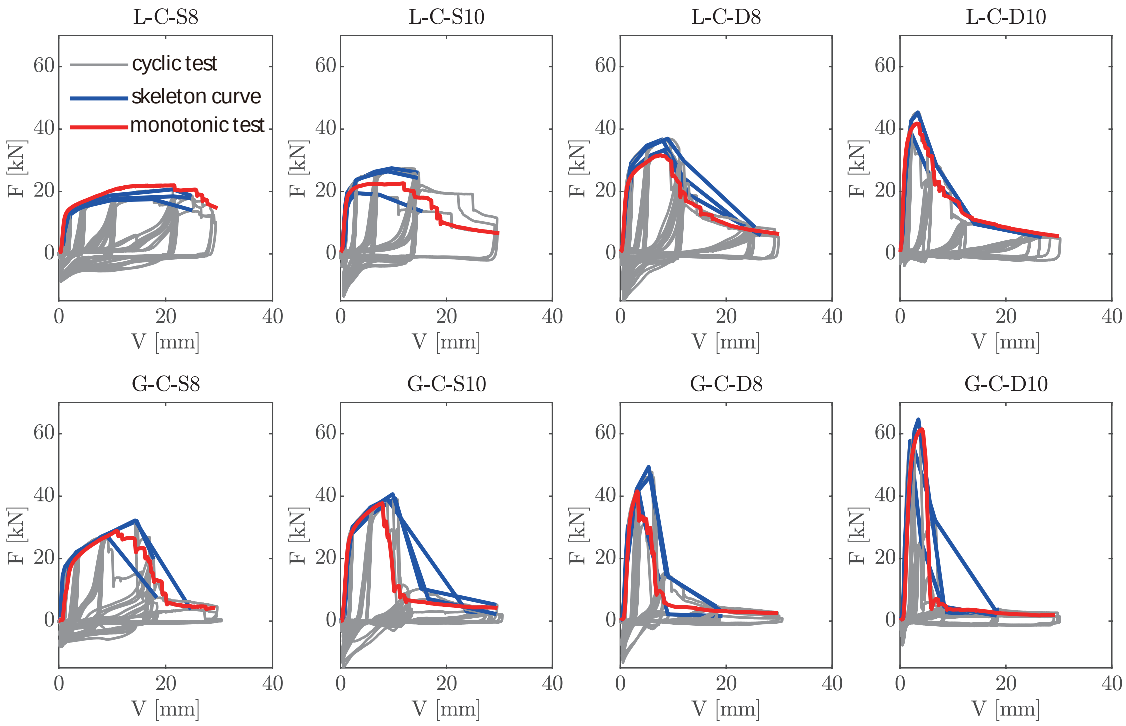

Figure 6: Load (F in kN) vs. displacement (V in mm) curve of cyclic loading tests. The first row refers to tests performed on LVL while the second reefers to glubam. The first two columns refers to single bolt and the last two to double bolts cases. The three gray lines are the three tests repetitions. The three blue lines are the skeleton curves of the three repetitions. The skeleton lines are calculated as the envelope of the cyclic tests. The red line is the average of three monotonic tests across displacements (see Figure 5). The average line ends when one of the test data is not available.

be attributed to the denser but thinner layers of LVL, resulting in a more homogeneous but softer material nature.

Table B.7 summarizes the initial stiffness, yield load, yield displacement, maximum load, and ultimate displacement, with statistical analysis performed on the results. The initial stiffness, yielding load, and maximum load capacity increase with increasing bolt diameter and number, while ductility exhibits an inverse relationship. Notably, the initial stiffness, yield load, and maximum load of D8 are generally higher, with lower ductility, compared to counterparts of S10, except for the initial stiffness of glubam. This finding suggests that the number of bolts have a strong influence on the observed mechanical properties more than the bolt diameter.

2.3.2. Cyclic loading

The hysteresis curves of three identical specimens of two types of materials (LVL and GLB) under cyclic loading are presented in Figure 6. As shown, the three replicates for each group of specimen exhibited similar response generally.

The equivalent viscous damping values, V_{eq}, obtained from experimental results for each cycle are presented in Figure 7(a). It can be observed that the equivalent viscous damping value is directly proportional to the diameter of the fastener. Moreover, the energy dissipation capacity of the system is significantly enhanced by doubling the number of fasteners. Generally, the equivalent viscous damping value increases with an increase in the number of loading cycles. However, the viscous damping during the initial loading cycles is considerably larger and not directly proportional to the cycle count due to the larger observed damage. The damping values shown in Figure 7(a) indicate that the equivalent viscous damping for both materials is primarily in the range of 0.03 to 0.3 and reaches its maximum value at approximately 12 to 15 cycles.

Figure 7(b) presents the variation of the total energy dissipation ΣE_{di} of the connections as a function of the loading cycles. It is notable that the energy dissipation of the component remains relatively constant during the initial loading cycles. However, during the later loading cycles, the energy dissipation of LVL connections increases at a faster rate compared to glubam connections. The total energy dissipation of all the bolted connections shows an approximate exponential relationship with the increase in loading cycles. The findings suggest that the energy dissipation capacity of LVL connections surpasses that of glubam connections. This is consistent with the higher ductility observed in Figure 7.

2.3.3. Failure modes

Figure C.24 presents failure modes and bolt deformation after test for a typical specimen in each group. The failure mode of bolted connections varies with material type and the number and diameter of the bolts adopted. The failure mode can be divided into shear failure and splitting failure. Moreover, the failure can happen after reaching embedded strength in the form of a combined failure mode [61, 62, 63, 64, 65] and/or formation of the plastic hinge in the bolt. LVL-S-8 connections present the highest ductility and tend to deform significantly with the formation of the plastic hinge (Table Appendix B) with embedment effect near the steel plate and large rope effect [47]. LVL-S-8 connections fail in the form of splitting crack, which could be related to the lower embedment strength and perpendicular-to-the-grain tensile strength (Table 1). LVL-S-10 connections exhibit a similar final crack pattern but a full embedment effect along the entire hole surface is observed. To sum up, LVL-S connections tend to fail in the form of splitting failure consistently with the literature [66].

Compared to LVL, GLB-S connections exhibit both shear failure and splitting failure without any dominating behavior without any embedment of the bolt in the block since glubam has much higher embedment strength compared with LVL (see Table 1).

Double bolted connections exhibit lower ductility but higher bearing capacity compared with single bolt connections (Table Appendix B). LVL-D-8 connections perform the best ductility among double bolted connections (same as for the single bolt case). The failure of LVL-D-8 always originates from a shear failure in the part between the two bolts, then followed by a splitting crack in the part above the first bolt (similar to the single bolt case). No evident differences were observed for LVL-D-10 connections tending to fail with a shear failure in the part between the two bolts and splitting above the first bolt. Similar to single bolt connections, GLB-D specimens exhibit both shear failure and splitting failure without any dominating behavior above the first bolt. Similar to LVL-D, shear failures in the part between the two bolts were observed in GLB-D tests.

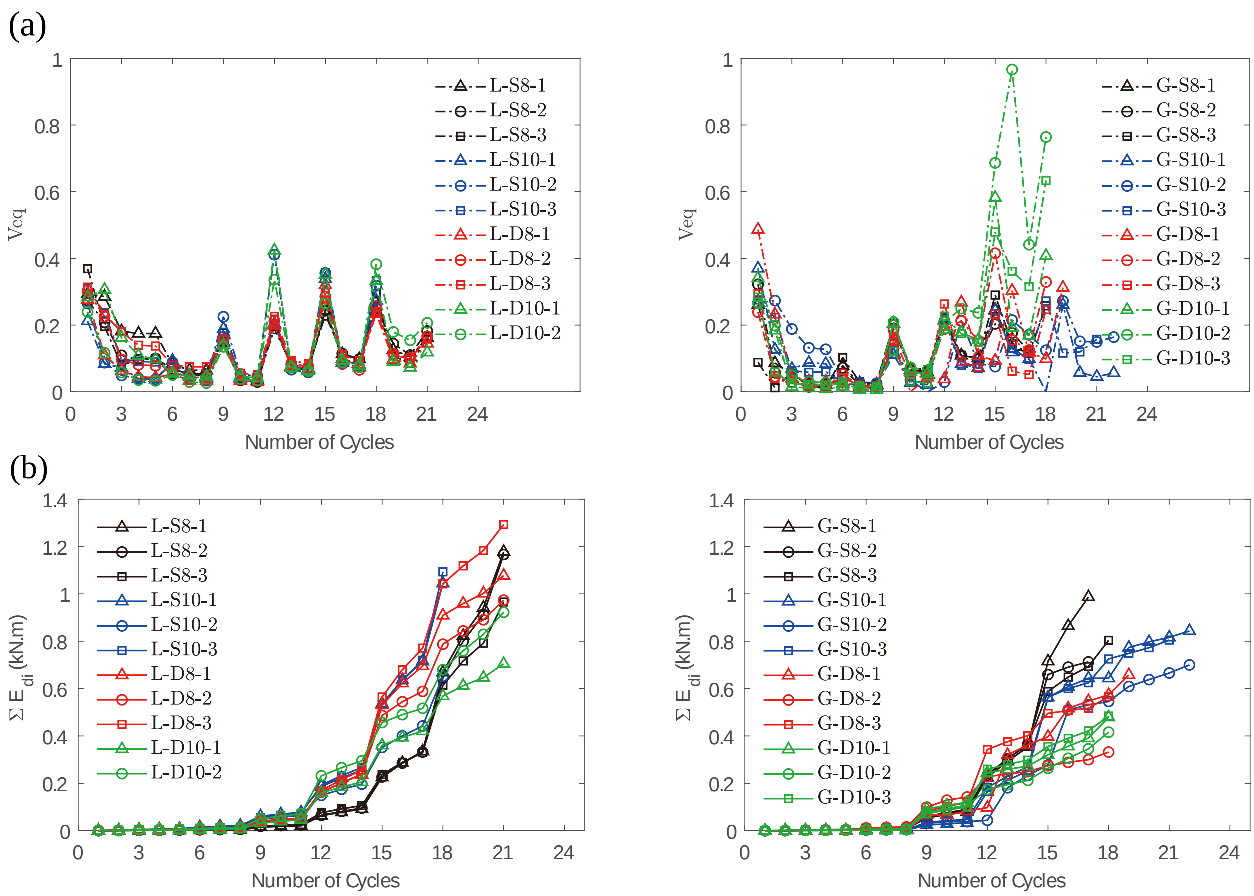

Figure 7: Equivalent viscous damping V_{eq} (a) and evolution of cumulative energy dissipation ΣE_{di} (b) with the increases of loading cycles. Lines with the same color refer to the three repeated test of the same configuration.

3. Finite element modeling

This Section describes the innovative finite element model proposed and reports the validation performed adopting the experimental results. Section 3.1 describes the material constitutive law adopted for LVL and glubam. In particular, Sections 3.1.1, 3.1.2, 3.1.3, and 3.1.4 describe the elastic behavior modeling, plastic

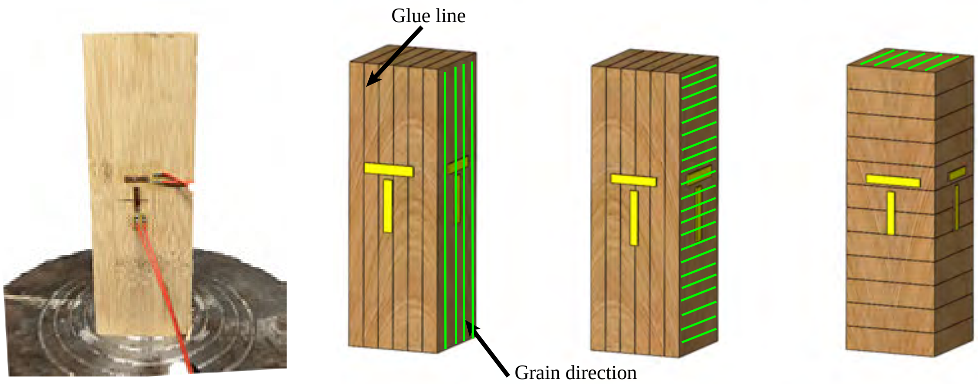

Figure 8: Specimen for elastic constants measurements. The green line shown in the sketch of specimen refers to the grain direction and the black line is the glue line of products.

Table 3: Engineering constants used in the ABAQUS model to define LVL and glubam elastic material (GPa).

	E_1	E_2	E_3	μ_{12}	μ_{13}	μ_{23}	μ_{21}	μ_{31}	μ_{32}	G_{23}	G_{13}	G_{12}
LVL	11.45	4.25	0.81	0.182	0.351	0.364	0.068	0.05	0.069	0.377	0.462	0.510
Glubam	8.56	5.65	2.81	0.282	0.336	0.316	0.180	0.160	0.157	0.410	0.568	0.612

behavior, effective foundation model properties, and crack modeling, respectively. Section 3.1.5 describes the utilization of ABAQUS user subroutine and the validation of materials constitutive law defined in subroutine. Section 3.2 describes the finite element implementation in ABAQUS. An assessment of the validity of the FE predictions is required, before the FE model can be further used for relevant investigations and engineering design analysis [67]. Finally, in Section 3.3, the 3D FEM model is validated against experimental load-displacement curves and experimental strain field.

3.1. Material constitutive law of LVL and glubam

3.1.1. Elastic behavior modeling

LVL and glubam are treated as orthotropic materials and their elastic behavior is modeled by stiffness matrix characterized by engineering constants [27, 28, 29]:

$$\boldsymbol{\sigma} = \mathbf{S}_{orth}\boldsymbol{\varepsilon} \tag{1}$$

where $\boldsymbol{\sigma}$ and $\boldsymbol{\varepsilon}$ are the vectors containing the stress and strain components, respectively, and $\mathbf{S}_{orth}$ is defined as:

$$\mathbf{S}_{orth} = \begin{bmatrix} \frac{1}{E_1} & \frac{-\mu_{21}}{E_2} & \frac{-\mu_{31}}{E_3} & 0 & 0 & 0 \\ \frac{-\mu_{12}}{E_1} & \frac{1}{E_2} & \frac{-\mu_{32}}{E_3} & 0 & 0 & 0 \\ \frac{-\mu_{13}}{E_1} & \frac{-\mu_{23}}{E_2} & \frac{1}{E_3} & 0 & 0 & 0 \\ 0 & 0 & 0 & \frac{1}{G_{12}} & 0 & 0 \\ 0 & 0 & 0 & 0 & \frac{1}{G_{13}} & 0 \\ 0 & 0 & 0 & 0 & 0 & \frac{1}{G_{23}} \end{bmatrix} \tag{2}$$

where E_1, E_2, andE_3 are the three Young's moduli, G_{12}, G_{23}, and G_{31} are the shear moduli, and μ_{12}, μ_{23}, and μ_{31} are the three Poisson's ratios. The subscripts 1, 2 and 3 indicates the three mutual orthogonal orientations.

LVL and glubam constants were determined performing experimental tests carried out using a compression testing machine [68]. The rate of loading is 2 kN/min. The dimension of the specimens was 60 mm × 20 mm × 20 mm. The layouts of the strain gauges on the specimens are shown in Figure 8. Six groups of six specimens were tested: three groups of compressive specimens in X, Y, and Z directions (matching the 1, 2, and 3 directions in Eq. 2) for measuring Young's moduli; three groups of 45° eccentric compression loading specimens for measuring the shear moduli.

All the measured constants are summarized in Table 3 where E, G, and μ refer to the modulus of elasticity, shear modulus, and Poisson ratio, respectively. Similar results were reported in the literature for LVL [69] and for glubam [50].

3.1.2. Plastic behavior modeling

The Hill's yielding criterion is adopted herein to characterize plastic behavior of orthotropic materials [46, 70, 71, 72], which takes into considerations material and yielding orthotropy [73]. The Hill's yielding criteria

Table 4: Input yield stresses for nonlinear behavior in ABAQUS model (MPa).

	$\bar{\sigma}_{11}$	$\bar{\sigma}_{22}$	$\bar{\sigma}_{33}$	$\bar{\sigma}_{12}$	$\bar{\sigma}_{13}$	$\bar{\sigma}_{23}$
LVL	38.91	14.03	13.23	6.27	6.27	5.53
Glubam	73.77	36.15	33.38	18.13	6.58	22.59

has been successfully applied in other researches such as CLT dowel-type connections [69], timber joints with glued-in rods [74] and traditional timber mortise-tenon joints [75]. The Hill's yielding criterion is defined by Hill's potential function where the input parameter is the yield stress ratio in each direction of orthotropic materials:

$$f(\sigma_{ii}) = \overline{\sigma} = \sqrt{F_{11}(\sigma_{22}-\sigma_{33})^2 + F_{22}(\sigma_{33}-\sigma_{11})^2 + F_{33}(\sigma_{11}-\sigma_{22})^2 + 2N_{23}\sigma_{23}^2 + 2N_{31}\sigma_{31}^2 + 2N_{12}\sigma_{12}^2} \quad (3)$$

where $\overline{\sigma}$ is the equivalent stress, σ_{11}, σ_{22} and σ_{33} are the normal stresses, σ_{12}, σ_{23} and σ_{31} are the shear stresses. F_{ii} and N_{ii} are constants obtained by tests of the material in different orientations, and are defined as follows:

$$F_{ii} = \frac{(\sigma^0)^2}{2}\left(\frac{1}{\overline{\sigma}_{jj}^2} + \frac{1}{\overline{\sigma}_{kk}^2} - \frac{1}{\overline{\sigma}_{ii}^2}\right) = \frac{1}{2}\left(\frac{1}{R_{jj}^2} + \frac{1}{R_{kk}^2} - \frac{1}{R_{ii}^2}\right), N_{ij} = \frac{3}{2}\left(\frac{\tau^0}{\overline{\sigma}_{ij}^2}\right)^2 = \frac{3}{2R_{ij}^2} \quad (4)$$

where σ^0 and τ^0 are reference yielding stresses defined by using the Mises plasticity definition syntax ($\tau^0 = \sqrt{3}\sigma^0$), $\overline{\sigma}_{ij}$ are the yielding stresses with respect to the axes of anisotropy from the pure uniaxial and shear tests, and R_{ij} are yield ratios which relate the yield level for stress component σ_{ij} to the reference yield stress σ^0 of the material. The yield ratios are defined as follows:

$$R_{11} = \frac{\overline{\sigma}_{11}}{\sigma^0}, R_{22} = \frac{\overline{\sigma}_{22}}{\sigma^0}, R_{33} = \frac{\overline{\sigma}_{33}}{\sigma^0}, R_{12} = \frac{\overline{\sigma}_{12}}{\tau^0}, R_{13} = \frac{\overline{\sigma}_{13}}{\tau^0}, R_{23} = \frac{\overline{\sigma}_{23}}{\tau^0} \quad (5)$$

The six yielding stresses are needed for defining the yielding criterion for the LVL and glubam: $\overline{\sigma}_{11}$, $\overline{\sigma}_{22}$, $\overline{\sigma}_{33}$, $\overline{\sigma}_{12}$, $\overline{\sigma}_{13}$ and $\overline{\sigma}_{23}$. In this study, the compressive yield strength was opted as the reference yield stress and the final yield stresses adopted are presented in Table 4.

For the orthotropic material plasticity, the associated flow rule used is given by:

$$d\{\varepsilon\}_{pl} = \lambda\left\{\frac{\partial f}{\partial\{\sigma\}}\right\}, \lambda = d\overline{\varepsilon}_{pl} = \frac{d\overline{\sigma}}{\overline{H}} \quad (6)$$

where λ is a proportionality constant termed the plastic multiplier, and $d\overline{\varepsilon}_{pl}$ and $d\overline{\sigma}$ are equivalent plastic strain and equivalent stress, respectively. $1/\overline{H}$ is a hardening modulus equal to the slope of $\overline{\sigma} - \overline{\varepsilon}_{pl}$ curve which can be obtained from embedment experiment (Figure 9).

In this study, for the laminated timber and bamboo elements in the embedment zone (the area around the bolt, see yellow area in Figure 14), wood foundation model was used to describe the local crushing behavior due to embedment compression. In wood foundation model, material hardening was considered by bi-linear fitting the performance curves obtained from the embedment compression tests and the test methods is shown in Figure 9 (b). As observed in Figure 9 (a), the fitted bilinear relationship (red line) is in a good agreement with the embedment test curves (both 8 and 10 mm-diameter dowel-bearing test are shown). The relative LVL and glubam constitutive in the embedment zone are then determined by the fitting result shown in Figure 9 (a) according to the analysis method proposed by Hong and Barrett [32]. The foundation modulus and foundation yield point are defined based on the load-embedment displacement curve from embedment compression tests. In the fitted bilinear curve, an initial slope and a break point between two linear regions were identified. The nominal foundation modulus and the nominal yield point can then be calculated as:

$$k = \frac{P_y}{W_y} \quad (7)$$

where k is nominal foundation modulus (MPa), P_y is the yield load in the bilinear load/unit length-embedment displacement curve (N/mm), and W_y is the yield deformation in the load/unit length-embedment displacement curve (mm).

3.1.3. Effective foundation model properties

In the wood foundation model, the nominal foundation modulus along parallel-to-grain directions ($E_{1,F}$ in Table 5) are determined according to experimental results as discussed above, while the effective foundation modulus [32] along other directions ($E_{2,F}$, $E_{3,F}$, etc.) are derived by proportional transformation using the same ratio of E_1 and $E_{1,F}$ as following:

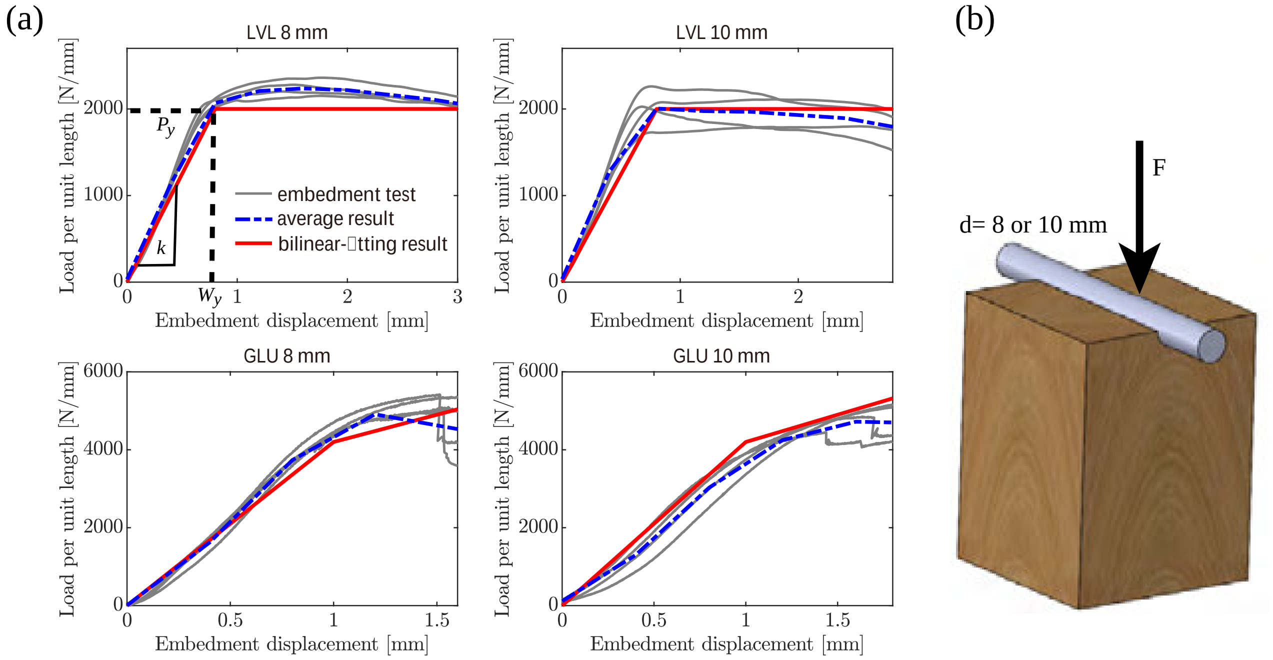

Figure 9: Embedment test: (a) load per unit length (in N/mm) vs. displacement (in mm) curves (gray line) and fitted bilinear constitutive law for wood foundation model (red line). The blue line is the average results of the test; (b) Embedment test method. k is nominal foundation modulus (MPa), P_y is the yield load in the bilinear load/unit length-embedment displacement curve (N/mm), and W_y is the yield deformation in the load/unit length-embedment displacement curve (mm), d is the diameter of bolt (mm).

Table 5: Engineering constants used in the user subroutine of ABAQUS to define wood foundation model for LVL and glubam (GPa).

Wood foundation model	$E_{1,F}$	$E_{2,F}$	$E_{3,F}$	$\mu_{12,F}$	$\mu_{13,F}$	$\mu_{23,F}$	$G_{23,F}$	$G_{13,F}$	$G_{12,F}$
LVL	2.5	0.93	0.18	0.182	0.351	0.364	0.08	0.10	0.11
Glubam	4.20	2.80	1.40	0.282	0.336	0.316	0.20	0.28	0.30

$$\frac{E_{1,F}}{E_1} = \frac{E_{2,F}}{E_2} = \frac{E_{3,F}}{E_3} \tag{8}$$

The Poisson's ratios in the wood foundation model ($\mu_{12,F}$, $\mu_{13,F}$, etc.) are the same as that obtained from the prism compression test (see Figure 8 and Table 3). The final parameters for the wood foundation model are listed in Table 5. It can be observed that the elastic constants in the three orthotropic directions are reduced significantly in the wood foundation model compared to the elastic constants reported in Table 3 directly obtained from prism compression tests. This is consistent with the approach proposed by Hong and Barrett [32] who adopted effective (reduced) foundation properties (i.e., properties of the material around the bolt) to match the observed stiffness.

3.1.4. Crack modeling

It can be seen from Figure C.24 that, the fracture of LVL and glubam, majorly the splitting crack in LVL and shear crack in glubam is the key factor leading to the failure of the connection. Although the softening behavior of LVL and glubam is simulated to some extent by Hill's yield criterion, no crack propagation is considered in this criterion. Herein, An attempt is made to simulate the cracking behavior by removing the damaged elements along the potential cracking zone (red areas in Figure 14) [27, 76]. To do this, a user subroutine, UMAT are integrated in ABAQUS to implement the damage function [34, 33] defined in Eq. 9. The damage variable D in Eq. 9 is utilized in the subroutine such that when its value reaches one, the subroutine passes the zero stress state to the element, and the element is deleted from the mesh. The size of the removed elements is about 0.1 mm wide and the total length is extended from the wall of bolt hole to the upper end of the member. The width of the removed elements is closed to the real crack width observed in the test and such a small width can also improve the calculation convergence. The area of the element removal is equal to the area of two shear failure plane and one splitting plane as shown in the red areas in Figure 14. The quantity of the removed elements is equal to the element quantity along these shear failure plane and splitting plane and when the block between two shear plane is totally sheared out (see Figure C.24 L-C-D8) or the block above the bolt is totally split (see Figure C.24 G-C-D10), the calculation will terminate.

$$D = \left(\frac{\overline{\sigma}}{f_{t,90}}\right)^2 + \left(\frac{\overline{\tau}}{f_{v,0}}\right)^2 \tag{9}$$

where $\overline{\sigma}$ and $\overline{\tau}$ are the perpendicular-to-grain tensile stress (σ_{22}) and parallel-to-grain shear stress (σ_{12}) respectively, and $f_{t,90}$ and $f_{v,0}$ are the perpendicular-to-grain tensile strength and parallel-to-grain shear strength respectively which can be obtained from previous material test results (Table 1).

The procedure for the element removal is:

1. Obtain perpendicular-to-grain tensile stress σ_{22} and parallel-to-grain shear stress σ_{12} from state variable in ABAQUS subroutine and check damage variable D.

$$D_e = \left(\frac{\sigma_{22,e}}{f_{t,90}}\right)^2 + \left(\frac{\sigma_{12,e}}{f_{v,0}}\right)^2 = 1 \tag{10}$$

   where e is an element number, which links to the elements to be checked.

2. An element is removed if it satisfies the condition in Eq. 10 by setting its material properties to zero. When the ii-th is removed, there will be a redundancy in the Jacobian matrix which will affect the tangential stiffness matrix $\boldsymbol{K}_T$:

$$\boldsymbol{K}_T = \begin{bmatrix} K^e_{11} & \cdot & \cdot & \cdot & K^e_{1i} & \cdot & \cdot & \cdot & K^e_{1n} \\ & \cdot & & & \cdot & & & & \\ & & & \cdot & \cdot & & & & \\ K^e_{i1} & \cdot & \cdot & \cdot & K^e_{ii} = 0 & & & & K^e_{in} \\ & & & & \cdot & \cdot & & & \\ & & & & \cdot & & & \cdot & \\ K^e_{n1} & \cdot & \cdot & \cdot & K^e_{ni} & \cdot & \cdot & \cdot & K^e_{nn} \end{bmatrix} \tag{11}$$

   where n is the total number of elements.

3. Start a new step based on a redundant structural tangential stiffness (i.e., remove the ii-th element associated rows and columns) and repeat steps 1 and 2.

3.1.5. ABAQUS user subroutine and FE material validation

A user subroutine, UMAT, is integrated in ABAQUS to implement the Hill's yielding criteria. This subroutine facilitates the implementation of the element removal criteria introduced in Section 3.1.4. The flowchart for a load increment and the implementation of Hill's yielding criteria and element removal criteria in the ABAQUS subroutine is shown in Figure 10.

To validate the feasibility of the Hill's yielding criterion in the UMAT subroutine, the compression test results of prism specimen are compared to the corresponding simulation results in ABAQUS as shown in Figure 11 and 12. In the modeling of the prism compression test, the material constitutive law of LVL and glubam is programmed in the subroutine according to the flowchart in Figure 10. The materials constants and yielding stress ratio defined in Hill's yielding function are adopted from Table 3 and 4. The update of state variable (equivalent plastic strain $d\overline{\varepsilon}_{pl}$) in each load-increment step is performed according to the flowchart in Figure 10 as well, while the element removal criterion is not exerted herein and only the Hill's yielding behavior is verified. Figure 12 shows the elasto-plastic behavior of LVL and glubam prism specimen under compression. It can be seen that the simulated load-displacement curve is in good agreement with the tested results and the simulated yielding strength keeps good fit with tested values. Therefore, the Hill's yielding criteria is validated in material property issue and the UMAT can accurately describe the LVL and glubam plastic behavior.

Figure 13 compares the experimental and simulated results in one representative embedment test (see Figure 1) by using the constitutive model as described above. The material constitutive law of LVL is programmed in the subroutine according to the flowchart in Figure 10. The update of state variables (equivalent plastic strain $d\overline{\varepsilon}_{pl}$ and damage variable D) in each load-increment step is performed according to the flowchart in Figure 10. Both the element removal criterion and Hill's yielding criterion are considered herein. It can be seen that the simulated cracking path is in good agreement with the cracking path observed from test (see Figure 13 b and c). A descending stage due to cracking was observed in the FEM loading-embedment displacement curves (see red line in Figure 13 a). Therefore, the validity of the material constitutive developed in ABAQUS UMAT by integrating the Hill's yielding criterion with the element removal criterion is verified.

3.2. Finite element implementation

The bolted connection with slotted in steel plate is modeled in ABAQUS. The 3D FE model (FEM) consists of one steel plate, bolts and main members (LVL or glubam) as reported in Figure 15 (a). The geometry of the connection components are the same as the geometry of the tested specimens, see Figure 2. In order to simplify the model and reduce the computation burden, the bolted joint with 4 bolts at the bottom end is

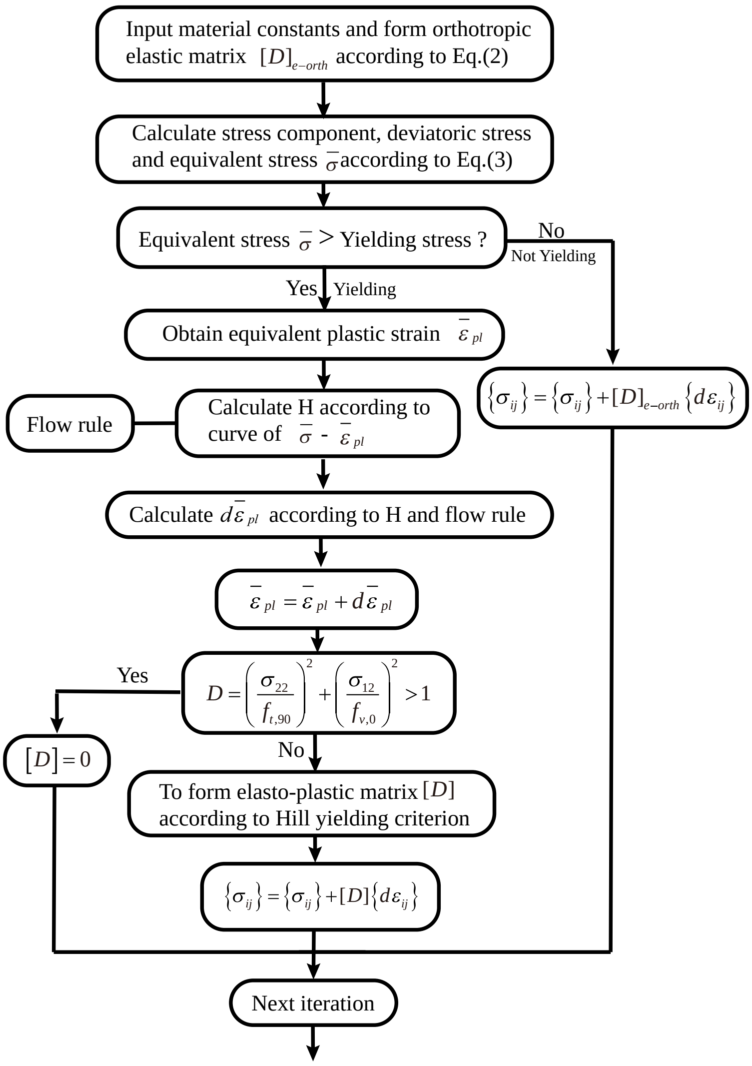

Figure 10: Flowchart for a load increment and implementation of Hill's yielding criterion and element removal criterion in the ABAQUS subroutine.

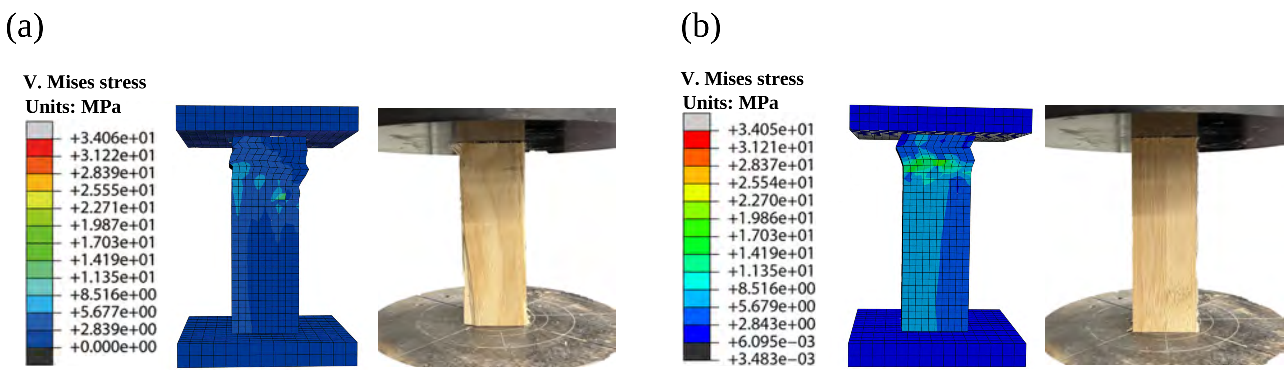

Figure 11: FEM model and simulated strain field in compression test of prism specimen: (a) LVL; (b) glubam.

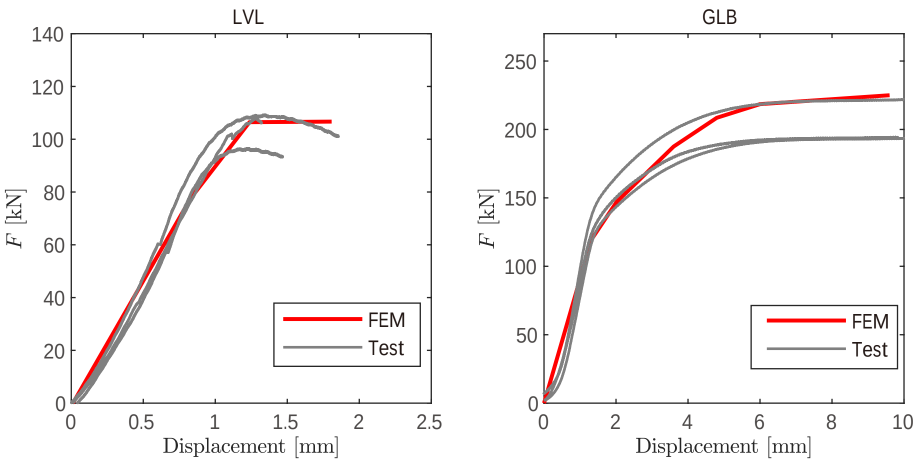

Figure 12: Tested and simulated load (F in kN) vs. displacement (in mm) curves in compression test of prism specimen: LVL (left) and GLB (right). The red line is the FEM result and the gray lines are three repeated test results.

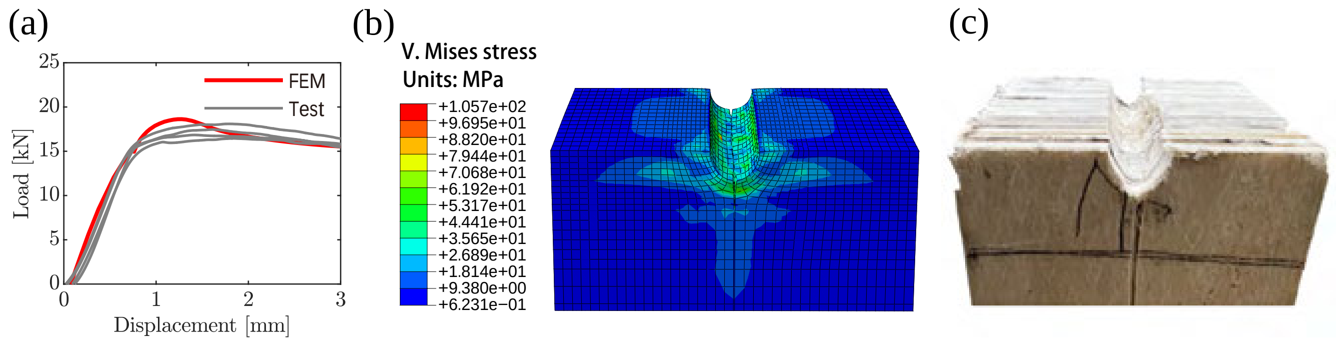

Figure 13: Simulated embedment test for LVL specimen with a 8mm-diameter half hole: (a) load (in kN) vs. embedment displacement (in mm) curve, the red line is the simulated result and the gray lines are four repeated test results; (b) simulated crack pattern and stress field; (c) experimental crack pattern.

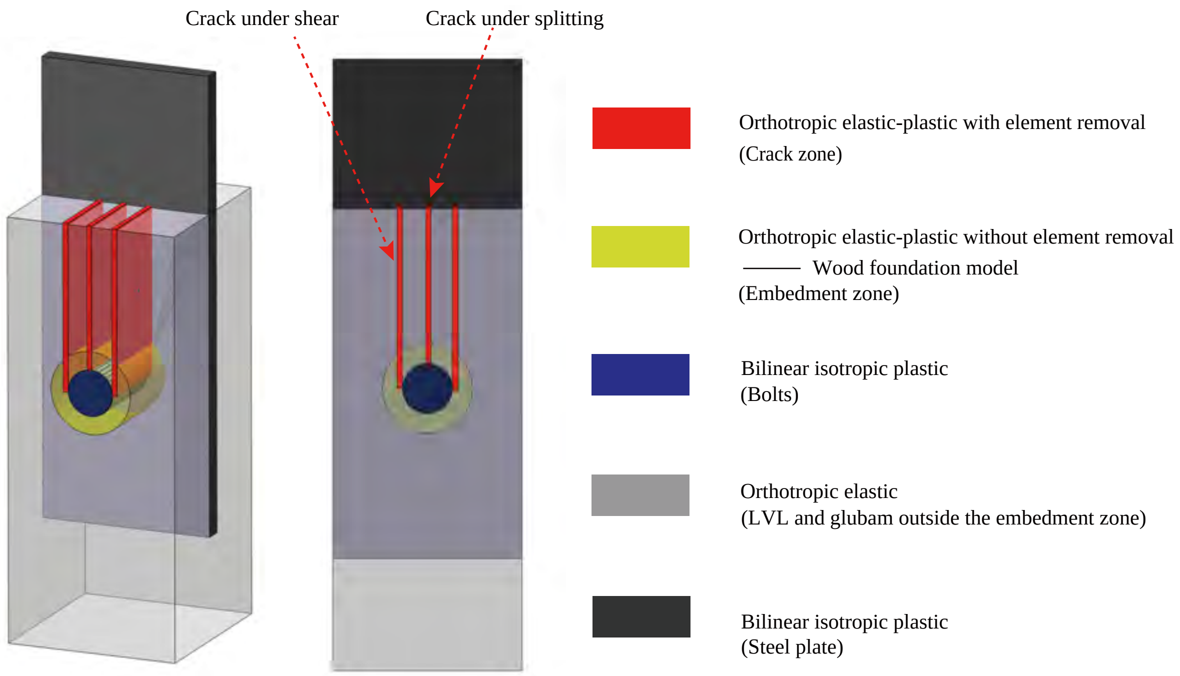

Figure 14: Material constitutive partitioning of the numerical model. The red area (crack zone) uses orthotropic elastic-plastic constitutive law with element removal; The yellow area (embedment zone) uses orthotropic elastic-plastic constitutive law without element removal; The blue area (bolt) uses isotropic plastic constitutive law; The gray area (outside the embedment zone) uses orthotropic elastic constitutive law; The black area (steel plate) uses bilinear isotropic plastic constitutive law.

not considered. Their displacement contribution is neglected since the LVDT only measures the displacements of the bolted joint at the upper end. This configuration of the FEM model can accurately simulate the real boundary conditions adopted in the tests.

All the components were modeled with eight-node brick elements (C3D8) in the ABAQUS software. The whole finite element model is shown in Figure 15 (a).

The bolt and steel plate was modeled as isotropic elastic-perfectly plasticity. For the bolts and steel plate, the module of elasticity (MOE) is 210 GPa and the Poisson ratio is 0.3 based on C10B21 steel properties [77]. The yield stress is 345 MPa for steel plate. The yield stress is 721.52 and 823.98 MPa respectively for $\Phi 8$ and $\Phi 10$ bolts, respectively, see Table 1.

It has been proved from previous studies [32, 75, 78, 16] that the constitutive of the elements outside the embedment zone (gray area in Figure 14) is negligible while that in the embedment zone (see red area in Figure 14) is dominating the response. Therefore, the LVL or glubam block is modeled with different material properties for elements inside and outside the embedment zone, and crack zone. The material partitioning of the block is shown in Figure 14. The elements outside the embedment zone (gray area in Figure 14) were assumed to be orthotropic linear elastic elements, and the Young's modulus was determined by compression tests of prism specimen (see Table 3). An adaptive mesh is adopted with mean mesh-size equal to around to 3 mm. The properties of these region are consistent with the description reported in Section 3.1.1. In the embedment zone, orthotropic elastic-plastic constitutive (Hill's yielding criteria) was used and the Hill's yielding criteria were implemented by directly inputting the parameter of Hill's yielding function in the ABAQUS user interface without establishing subroutine. The material properties in the embedement zone are equal to the effective foundation model properties (Section 3.1.3). As for elements in crack zone (red area in Figure 14), orthotropic elasto-plastic constitutive (Hill's yielding criteria) with progressive element removal was implemented. In the crack zone, the Hill's yielding criteria and element removal were both implemented by establishing subroutine. The thickness in the crack zone was set equal to 0.1mm and the mesh-size equal to around to 3 mm. The material parameters of the glubam and LVL refer to the experimental results in Section 3.1.

The interface property of all the contact surfaces is set as hard contact. The Coulomb friction coefficient of all the contact surfaces is taken as 0.5. Moreover, to model the initial slip stage caused by the hole clearance between the bolt and hole wall of timber elements [39], 0.5 mm tolerance between the interface of bolt and timber elements in ABAQUS model is set.

The simulation results of the failure modes obtained by the FEM (G-M-S10) are shown in Figure 15 as example. A typical shearing-out failure mode can be observed, which is consistent with the test observation (see Figure C.24). Moreover, a comparison of element status in the predetermined crack plane as fracture propagates is shown in Figure 16. It can be seen that the vanishing elements on the fracture plane gradually formed the

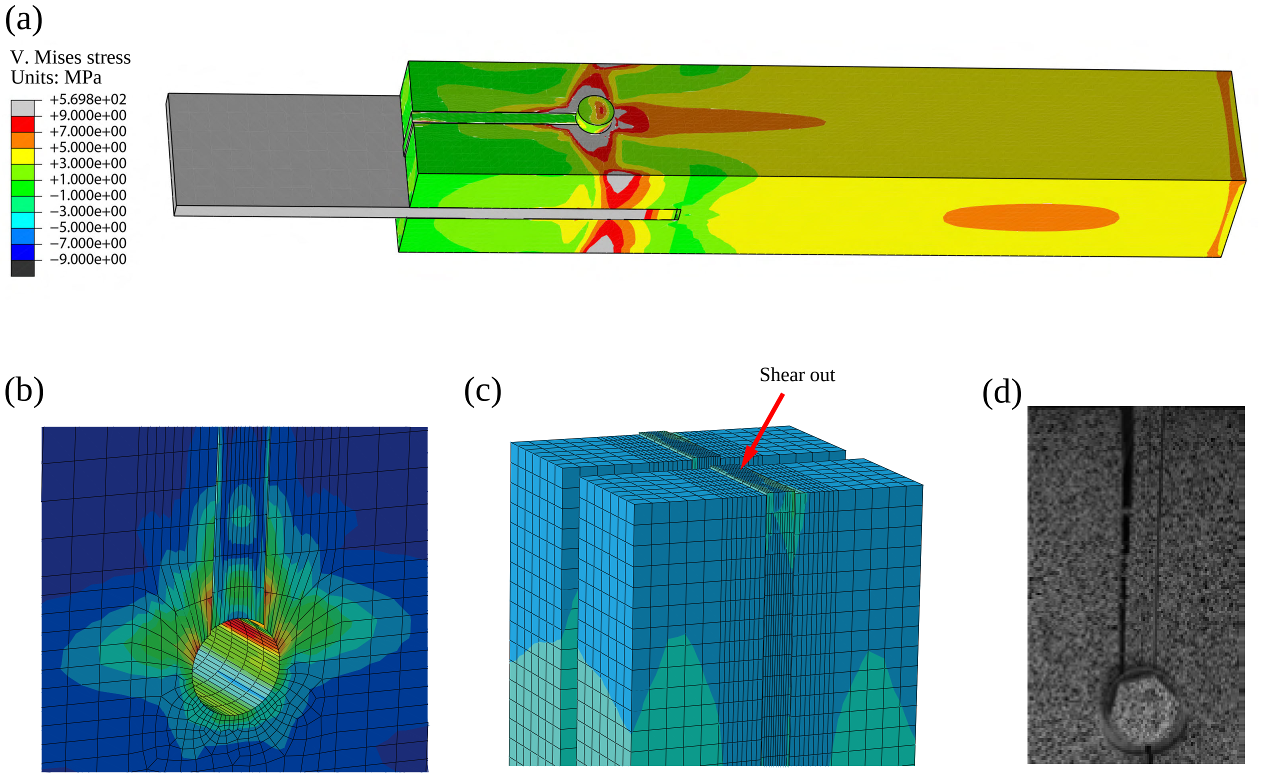

Figure 15: Comparison between simulated failure modes and tested failure modes of G-M-S10: (a) the whole finite element model; (b) strain field around the crack; (c) simulated shear-out failure; (d) shear-out failure from test.

final fracture path.

3.3. Validation of the FEM model

3.3.1. Load-displacement behavior

The load-displacement results of the FEA are shown in Figure 17 and 18. The comparison between the numerical and experimental load-displacement curves shows that the numerical model represents well the experimental curve. The numerical model is in good agreement with experimental observation regarding the main parameters such as the stiffness and the maximum load (F_u) in the case of monotonic loading (see Table D.8). The initial stiffness and maximum load capacity obtained from the experimental results and numerical model are compared further to the current European standards EC5 [79]. According to EC5 [79], the characteristic load-carrying capacity, $F_{v,Rk}$, of a steel-to-timber connection is formulated as follows:

$$F_{v,Rk} = \min \begin{cases} f_{h,k} t_1 d & (1) \\ f_{h,k} t_1 d \left[\sqrt{2 + \frac{4M_{y,Rk}}{f_{h,k} \cdot d \cdot t_1^2}} - 1 \right] & (2) \\ 2.3\sqrt{M_{y,Rk} \cdot f_{h,k} \cdot d} & (3) \end{cases} \tag{12}$$

where $M_{y,Rk}$ is the characteristic yield moment of the dowel, $f_{h,k}$ is the embedment strength of the timber member obtained from the material test, t_1 is the thickness of the member, and d is the diameter of the dowel. However, Eq. 12 specified in Eurocode 5 [79] only applies to single-bolted case. An effective bolts factor n_{ef} specified in Eurocode 5 [79] needs to be applied to calculate the maximum load for double-bolted cases:

$$F_{v,Rk} = n_{ef} F_{v,Rk} \tag{13}$$

For steel to timber joints, Eurocode 5 [79] also provides the following empirical formula to calculate the initial stiffness k_e per shear plane per fastener:

$$k_e = 2\rho^{1.5} d/23 \tag{14}$$

where k_e is the initial stiffness and ρ is the wood or bamboo density in kg/m^3. Since the investigated members have two shear planes in total, the initial stiffness of the connections can be predicted as:

$$k_e = n \cdot 4 \cdot \rho^{1.5} d/23 \tag{15}$$

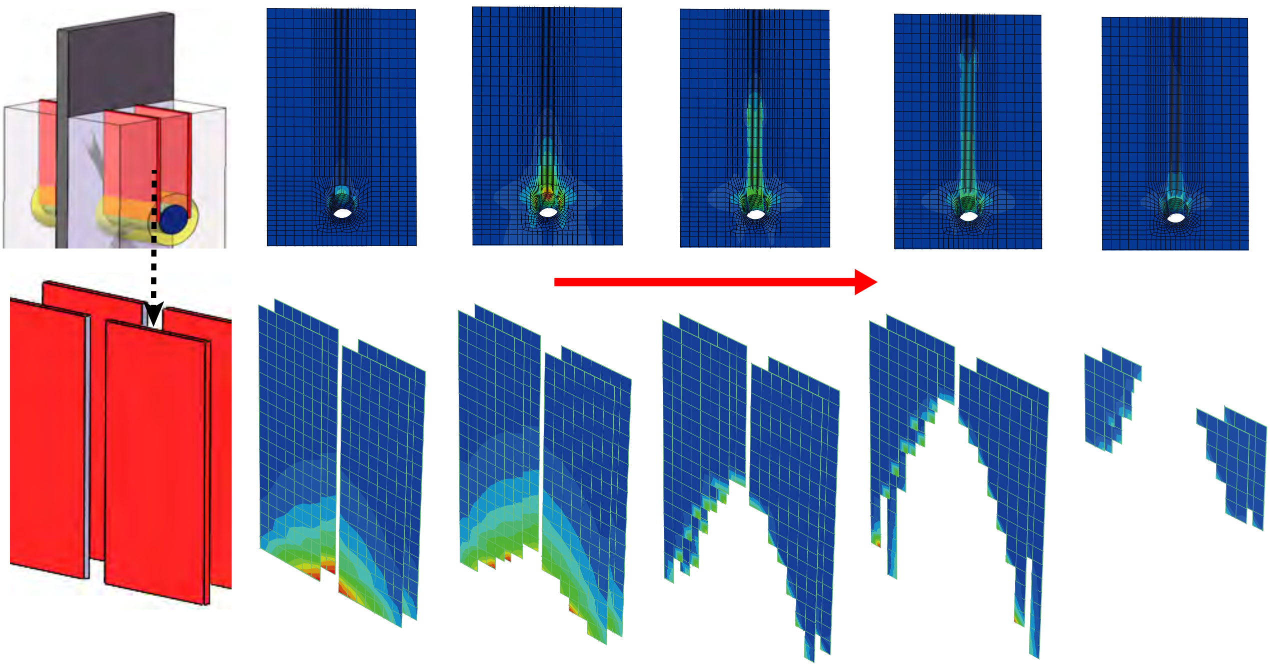

Figure 16: Evolution of element status in the pre-determined crack plane as fracture propagates.

The average initial stiffness and maximum load of the tested specimens, FEM results, and predicted results by EC5 [79] under monotonic loading are summarized in Table D.8. The results indicate that the initial stiffness of the connection is slightly higher in the FEM compared to the experimental results, which may be due to the tolerance between hole and fastener diameter. In the case of monotonic loading, the maximum load of the FE model meets the actual specimen peak load with a margin of error of 4%. As shown in Figure 18, the cyclic hysteretic loops predicted by the FEM appear to closely follow the shape of the experimental loops. The numerical initial stiffness and experimental elastic stiffness taken from the unloading-reloading phases are quite similar. To evaluate the ductility of the tested specimens under monotonic loading, the average ductility was compared with finite element method (FEM) results, as presented in Table D.8. With the exception of the L-MD10 and G-MD10 cases, the relative error in the remaining cases was confined within 20%. The observed discrepancy may be attributed to the larger diameter and number of bolts employed in these two cases, which resulted in the rapid propagation of cracks. This phenomenon is inconsistent with the progressive process predicted by the element removal criterion.

The formula from EC5 [79] predicts the initial stiffness and maximum load very well for single-bolted cases, while the prediction to double-bolted cases is not very accurate. A correction factor should be further considered to make Eqs. 13 and 15 applicable to double-bolted cases of LVL and glubam connections. This will be discussed in detail in Section 4.

3.3.2. Maximum principal strain field

Full-field strain data from Digital Image Correlation (DIC) provides rich information for FE analysis validation. Hybrid FEM-DIC method has been widely adopted in the structural analysis [27, 80] and validation of numerical model itself [81, 82, 83]. Figure 20 shows the full field strain distribution (maximum principal strain field) on surfaces of two representative specimens (LVL-D8-3 and GLB-D8-1) obtained from FEM analysis and DIC analysis at the pre-fracture point. Regarding DIC analysis, the selected surface is the side where the first crack is occurring. It can be seen that the prediction of the stress concentration area by FEM is in good agreement with measured results by DIC. The peak strain tends to lie in the middle line of surface (see Figure C.24 L-M-D8) or localize between the net and gross shear lines (see Figure C.24 L-M-S10) [84, 85]. This is consistent with the observed two types of failure mode, shear and splitting failure [86, 87, 88, 62, 89]. Additionally, it can be reflected by the strain distribution of bolt head that the rope effect can be modeled by the proposed FEM model.

Maximum principal strain of the surface elements obtained from the FEM model was compared with the DIC measurements mainly at three typical sections (1-1, 2-2 and 3-3), as shown in Figure 20. The validation is highlighted with 3 stages of the loading application, which are identified by 3 characteristic points A, B and C representing elastic phase, yield phase and peak load phase respectively as shown in Figure 19. From Figure 20, it can be seen that the evolution pattern of strain at the typical section obtained from the FEM is similar to DIC results. More specifically, the strain values derived from the FEM model at specific locations have

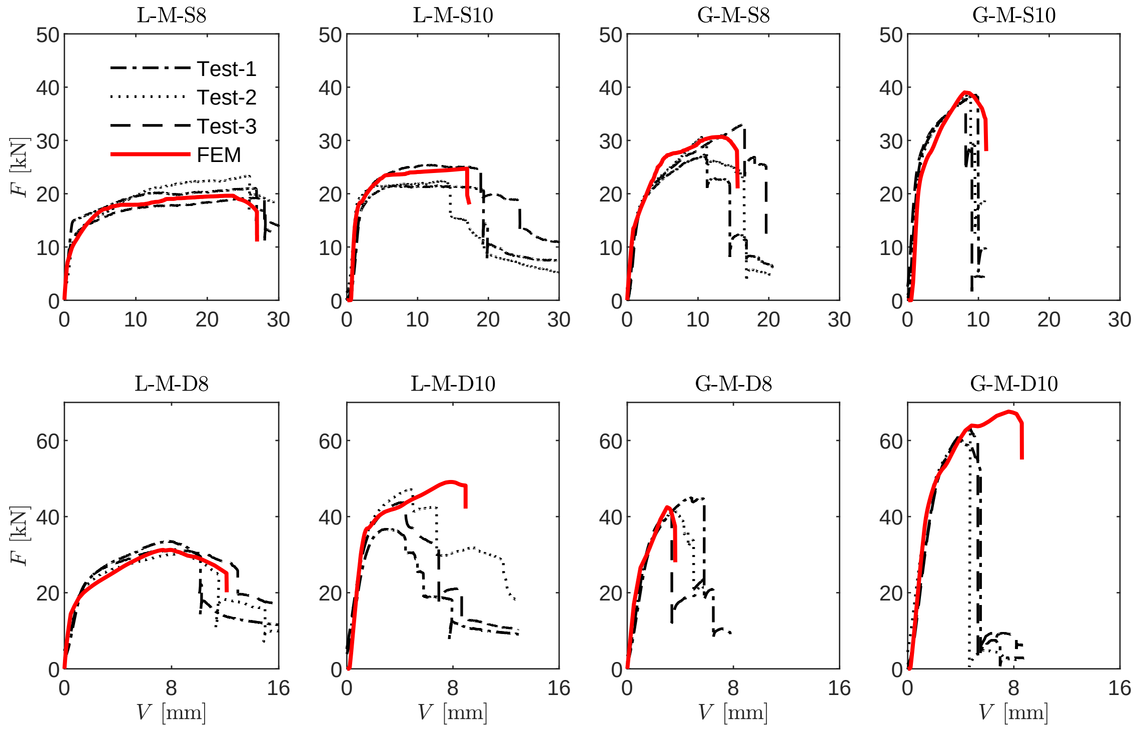

Figure 17: Load (F in kN) vs. displacement (V in mm) results of FEM analyses compared to experimental results under monotonic loading. The red line is the FEM result and gray lines are three repeated test results. The first two columns refers to results of LVL while the last two refers to glubam. The first row refers to single bolt and the second refers to double bolts cases.

allowable error compared to the DIC results. Generally, the strain values obtained by FEM are larger than DIC measurements since the strain obtained by FEM is not pure surface strain but reflects a certain inner strain, given that the studied surface elements in FEM model are hexahedral whose thickness is near 6 mm.

The evolution of the strain at the typical sections shows bimodal or unimodal patterns at sections 2-2 and 3-3, corresponding to active splitting planes and two active shear planes, respectively. Regarding section 1-1, the peak strain mainly localizes in the part between two bolts, which is consistent with experimental observations. In the experiment, the region between two bolts always cracked first, leading to the final failure of the specimen.

4. Theoretical analysis of elastic stiffness

This Section presents a theoretical analysis of elastic stiffness based on the FE analyses. Sections 4.1 and 4.2 reports a theoretical analysis of the elastic stiffness of single-bolted and double-bolted connections, respectively. Finally, Section 4.3 reports a validation of the proposed theoretical analysis of elastic stiffness by comparing with experimental, FE, and code-based (Eurocode 5) predictions.

4.1. Elastic stiffness of single-bolted connections

Yingyang and Jiajia [90] derived the initial stiffness model of single-bolted connections referring to the Winkler foundation model [91, 92, 93]. In the model of Yingyang and Jiajia [90], only half part is taken for analysis due to structural symmetry (Figure 21(a)). The axis direction and origin are shown in Figure 21(b). The bolt micro-segment at any x position is taken for analysis and the corresponding free body diagram is shown in Figure 21(c). In Figure 21, x represents the distance between a certain point and the midpoint on the bolt shank, which is positive to the right. w represents the deflection of bolt shank, which is positive upward. M and Q represent the moment and shear force of the bolt shank, respectively. The parameters involved in the derivation include the moment of inertia of bolt section, I, elastic modulus of bolt, E, and dowel-bearing stiffness of timber, k_s.

According to the equilibrium in the ω direction:

$$\frac{dQ}{dx} + k_s \omega(x) = 0 \tag{16}$$

According to the relationship between shear force, bending moment, and curvature of an Euler beam, the following equation can be obtained:

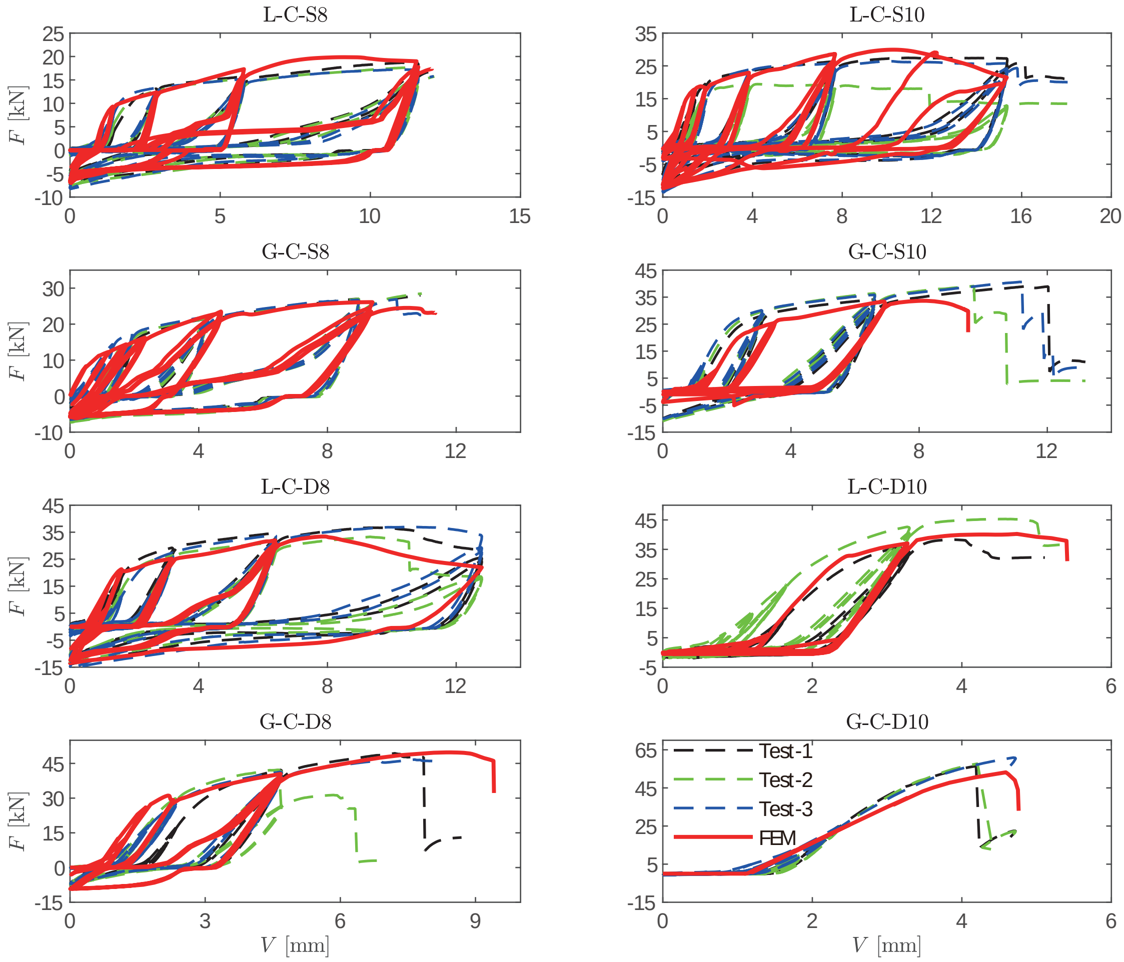

Figure 18: Load (F in kN) vs. displacement (V in mm) results of FEM analyses compared to experimental results under cyclic loading. The red line is the FEM result, and black, green and blue lines are three repeated test results. The first row refers to single-bolted LVL cases; the second row refers to single-bolted glubam cases; the third row refers to double-bolted LVL cases; the fourth row refers to double-bolted glubam cases.

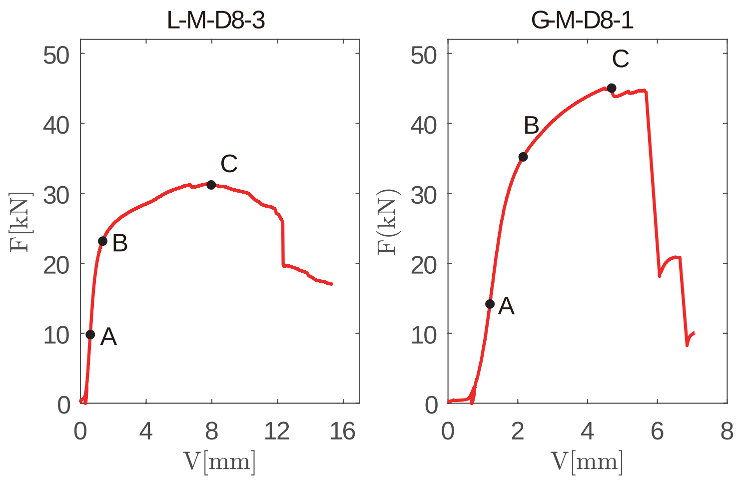

Figure 19: Definition of three characteristic points in the in load-displacement curve: A (limit of elastic phase), B (limit of yielding phase) and C (peak load phase).

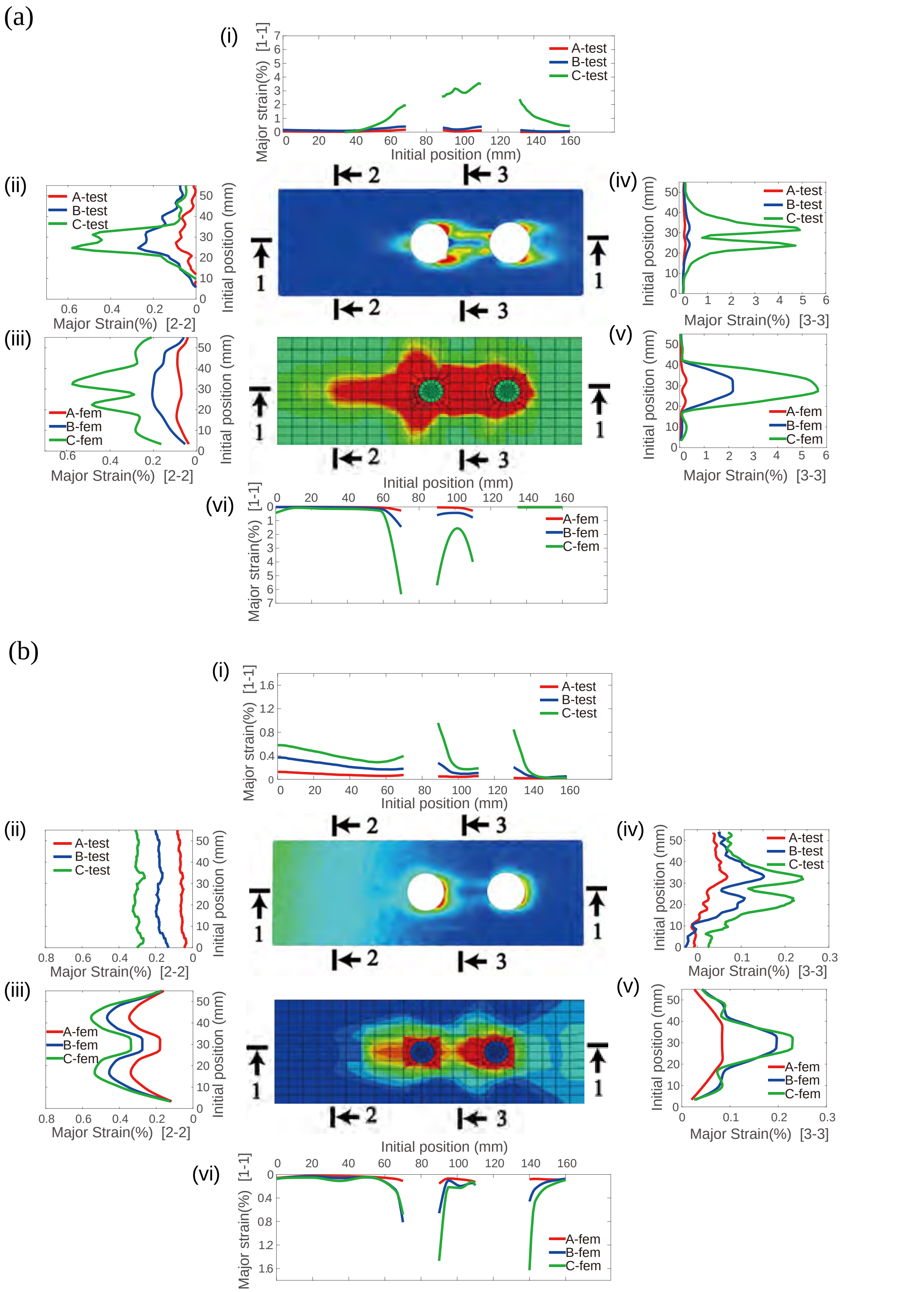

Figure 20: Comparison of sectional strain distribution between numerical and measured results by DIC: (a) LVL-D8-3; (b) GLB-D8-1. The red line shows the tested strain and simulated strain corresponding to A stage of Figure 19, blue line corresponds to B stage of Figure 19, and green line corresponds to C stage of Figure 19. The strain diagram (i) and (vi) show the strain evolution along Section 1-1 in the test and simulation results, respectively. The strain diagram (ii) and (iii) show the strain evolution along Section 2-2 in the test and simulation results, respectively. The strain diagram (iv) and (v) show the strain evolution along Section 3-3 in the test and simulation results, respectively.

$$\frac{d^4\omega(x)}{dx^4} + \frac{k_s}{EI}\omega(x) = 0 \tag{17}$$

Assuming $l_c = \sqrt[4]{4EI/k_s}$ and $\xi = x/l_c$, the following equation can be obtained:

$$\frac{d^4\omega(\xi)}{d\xi^4} + 4\omega(\xi) = 0 \tag{18}$$

The solution to the above homogeneous differential equation can be written as:

$$\omega(\xi) = A_1 e^{\xi}(\cos\xi + i\sin\xi) + A_2 e^{\xi}(\cos\xi - i\sin\xi) + A_3 e^{-\xi}(\cos\xi + i\sin\xi) + A_4 e^{-\xi}(\cos\xi - i\sin\xi) \tag{19}$$

where A_1, A_2, A_3, A_4 are constants. Assuming $B_1 = A_1 + A_2$, $B_2 = A_1 i - A_2 i$, $B_3 = A_3 + A_4$, $B_4 = A_3 i - A_4 i$, the following equation can be obtained:

$$\omega(\xi) = B_1 e^{\xi}\cos\xi + B_2 e^{\xi}\sin\xi + B_3 e^{-\xi}\cos\xi + B_4 e^{-\xi}\sin\xi \tag{20}$$

As x (that is, ξ) increases, the deflection ω gradually approach to 0 and the terms containing $e^{\xi}\cos\xi$ and $e^{\xi}\sin\xi$ in Eq. 20 diverge, thus $B_1 = B_2 = 0$.

Assuming $g_1 = e^{-\xi}\cos\xi$, $g_2 = e^{-\xi}\sin\xi$, $g_3 = g_1 + g_2$, $g_4 = g_1 - g_2$, thus $\frac{dg_1}{d\xi} = -g_3$, $\frac{dg_2}{d\xi} = g_4$, $\frac{dg_3}{d\xi} = -2g_2$, $\frac{dg_1}{d\xi} = -2g_1$. The deflection ω, rotation angle θ, moment M, shear force Q at certain x position can be obtained as:

$$\omega(\xi) = B_3 g_1 + B_4 g_2, \theta(\xi) = \frac{d\omega(x)}{dx} = \frac{1}{l_c}(-B_3 g_3 + B_4 g_4) \tag{21}$$

$$M(\xi) = EI\frac{d^2\omega(x)}{dx^2} = \frac{2EI}{l_c^2}(B_3 g_2 - B_4 g_1), Q(\xi) = \frac{dM(x)}{dx} = \frac{2EI}{l_c^3}(B_3 g_4 + B g_3) \tag{22}$$

At $x = 0$ ($\xi = 0$), there is shear force Q_0, moment M_0, and when substituted into Eq.22, one can solve as:

$$B_3 = \frac{l_c}{2EI}(l_c Q_0 + M_0), B_4 = \frac{-l_c}{2EI}M_0 \tag{23}$$

Thus Eqs. 21-22 can be expressed as:

$$\omega = \frac{l_c^2}{2EI}(l_c Q_0 g_1 + M_0 g_4), \theta = \frac{-l_c}{2EI}(l_c Q_0 g_3 + 2M_0 g_1) \tag{24}$$

$$M = l_c Q_0 g_2 + M_0 g_3, Q = Q_0 g_4 - \frac{2}{l_c}M_0 g_2 \tag{25}$$

The elastic stiffness k_e of the bolt joint can be described as the ratio of the external force F to the displacement V of bolt shank at the midpoint. It could be approximately considered that $V \approx \omega_0$.

At $x = 0$ ($\xi = 0$), the shear force is $Q_0 = 0.5F$ and when substituted into Eq. 24, the following equation can be obtained:

$$V = \omega_0 = \frac{l_c^2}{2EI}\left(l_c\frac{F}{2} + M_0\right) \tag{26}$$

Assuming

$$\beta_1 = \frac{1}{\left(1 + 2\frac{M_0}{l_c F}\right)} \tag{27}$$

The elastic stiffness k_e of the bolt joint can be calculated as follows when substituting $l_c = \sqrt[4]{4EI/k_s}$ into Eq. 26.

$$k_e = \frac{F}{V} = \beta_1\left(k_s\sqrt[4]{\frac{4EI}{k_s}}\right) \tag{28}$$

where $k_s = k_{h,0}d$ and EI are determined adopting material properties (see Table 1) and geometric dimensions.

The determination of β_1 is discussed as follows:

1. When the rotation of the mid-point of bolt shank ($x = 0$) is fully constrained ($\theta_0 = 0$), substituting ($\theta_0 = 0$) into Eqs. 24 and 27, one can solve that $\beta_1 = 2$;

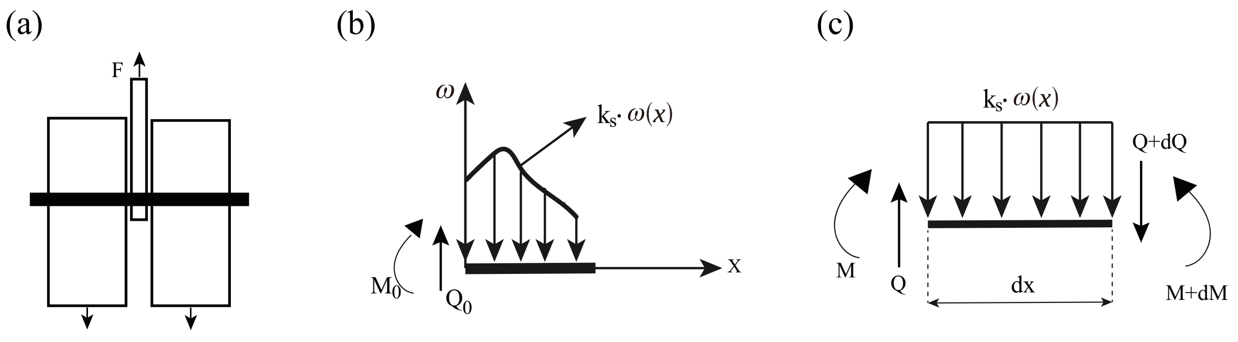

Figure 21: Force analysis of bolt shank: (a) diagram of bolt joint; (b) free body diagram of half bolt shank; (c) free body diagram of micro unit of bolt shank. M and Q represent the moment and shear force of the bolt shank, respectively. k_s represents the dowel-bearing stiffness of LVL or glubam block.

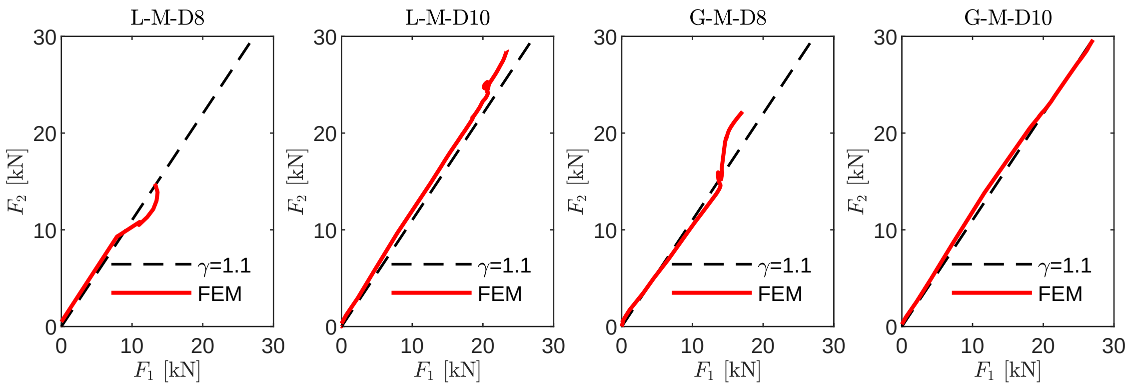

Figure 22: Comparison of the load born by the first bolt and the second bolt derived from the FE model. The red line is the relationship between F_1 and F_2obtained from FEM analysis, and the black dashed line is the reference line with a slope of 1.1.

2. When the rotation of the mid-point of bolt shank ($x = 0$) is not fully constrained ($M_0 = 0$), substituting ($M_0 = 0$) into Eq. 27, one can solve that $\beta_1 = 1$.

Therefore, β_1 is ranging between 1 and 2. During the elastic stage, β_1 can be approximately taken as 2, since the rotation of the mid-point of the bolt shank is small.

4.2. Elastic stiffness of double-bolted connections

In double-bolted connections, the applied total load F on the bolted connections can be considered as the sum of the load applied on the first bolt F_1 and the load applied on the second bolt F_2. From the numerical analysis, the load distributions on each bolt were obtained by summing the force of elements in contact with the bolt along the length of the bolt, and the contact force on the wood-to-bolt interface in the parallel to grain direction could be output from FE model developed in ABAQUS. The values of F_1 and F_2 obtained from the FE analyses for different configurations are listed in Figure 22. According to Figure 22, the ratio of the forces on the two bolts is $\gamma = F_2/F_1 \approx 1.1$.

At $x = 0$ ($\xi = 0$), the shear force is $Q_0 = 0.5F_1 = F/\left[2\left(1+\gamma\right)\right] = F/4.2$ and when substituted into Eq. 24, the following equation can be obtained:

$$V - \phi_v = \omega_0 = \frac{l_c^2}{2EI}\left(l_c\frac{F}{4.2} + M_0\right) \tag{29}$$

It is noteworthy that the deflection ω_0 of the first bolt hole at $x = 0$ in double bolted connections is no longer equal to the total displacement V as in the single bolted case (see Eq. 26). A corrected deflection term ϕ_v has to be subtracted from V to get the final deflection of the first bolt hole at $x = 0$, since the force from the second bolt F_2 has caused certain movement of the cross-section aligning with the first bolt hole. ϕ_v can be obtained as:

$$\phi_v = \frac{F_2}{E_0A}L = \frac{F}{1.9E_0A}L \tag{30}$$

where E_0 is the parallel-to-grain elastic modulus of glubam and LVL, A is the cross-sectional area of the member ($60 \times 60\,\mathrm{mm}^2$), and L is the distance between the fixed end and the cross-section aligning with the first bolt

Table 6: Comparison of the elastic stiffness from experimental tests, FEM analyses, and proposed theoretical model. The error is calculated as the difference between the considered variable and $k_{e.Test}$ normalized by $k_{e.Test}$. $k_{e.Test}$ is the average elastic stiffness measured from the tests (see Table B.7). $k_{e.FEM}$ is the elastic stiffness determined from the FE analyses. $k_{e.Theo}$ is the elastic stiffness calculated using proposed theoretical model.

	Units	L-MS8		L-MS10		G-MS8		G-MS10		L-MD8		L-MD10		G-MD8		G-MD10	
		value	error	value	error	value	error	value	error	value	error	value	error	value	error	value	error
$k_{e.Test}$	kN/mm	20.29	—	24.61	—	24.48	—	37.48	—	30.28	—	46.22	—	33.33	—	49.70	—
$k_{e.FEM}$	kN/mm	17.76	-12%	26.52	8%	26.24	7%	36.33	-3%	28.89	-5%	51.36	11%	32.53	-2%	47.54	-4%
$k_{e.Theo}$	kN/mm	17.89	-12%	27.85	13%	28.74	17%	34.98	-7%	32.99	9%	48.10	4%	46.46	39%	53.86	8%

hole, equal to 290 mm (see Figure 2(b)).

Assuming

$$\beta_2 = \frac{1}{1 + 4.2\frac{M_0}{l_c F}} \tag{31}$$

The elastic stiffness, k_e, of the bolt joint can be calculated as follows when substituting $l_c = \sqrt[4]{4EI/k_s}$ and Eq. 30 into Eq. 29.

$$k_e = \frac{F}{V} = \beta_2 \left(\frac{2.1 \cdot 1.9E_0 A k_s \sqrt[4]{\frac{4EI}{k_s}}}{1.9E_0 A + 2.1\beta_2 L k_s \sqrt[4]{\frac{4EI}{k_s}}} \right) \tag{32}$$

The determination of β_2 is similar to β_1 (see Section 4.1). Therefore, for small displacements, β_2 can also be approximately taken as 2.

4.3. Validation

Table 6 shows the theoretical elastic stiffness values of the bolted connections studied here, obtained by substituting the material property parameters from Table 6 into Eqs. 28 and 32. Moreover, Table 6 summarizes the experimental value, simulated value from FEM and theoretical value of elastic stiffness. The theoretical values and the simulated value from FEM show a better fit to the test results. It is found that the theoretical values of elastic stiffness are in good agreement with the test results. Comparing Tables 6 and D.8, it can be observed that the prediction of the proposed model over-perform the predictions of Eurocode 5. These findings suggest that the theoretical formula proposed in this study is effective in predicting initial stiffness.

5. Conclusions

The present study investigates the mechanical performance of bolted steel connections to laminated timber and bamboo composite members with slotted-in steel plates. The study compares the mechanical response of two different laminated composite bio-based materials for the first time, and characterizes their cracking modes and hysteretic responses. The study also implements a user-defined constitutive subroutine into a ABAQUS FE code to simulate the 3-dimensional structural behavior of the connections, and proposes a material constitutive integrating Hill's yielding criteria with element removal criteria for predicting brittle fracture.

The results show that the response of the bolted steel connections strongly depends on the number and diameter of bolts and the material employed (LVL and glubam). LVL connections exhibit greater ductility and energy dissipation capacity compared to glubam connections, which generally exhibit brittle behavior and higher peak strength. The FE simulations are found to be in good agreement with the experimental results, and the proposed material constitutive with element removal is shown to effectively simulate crack growth and predict brittle fracture. The study also provides theoretical formulas for bolt joint stiffness that can be used as a reference for the development of design guidelines for such connections.

Acknowledgments

This research is supported by the National Key Research and Development Program of China (2019YFD1101002). This work has been partially supported by the Zhejiang University/University of Illinois at Urbana-Champaign Institute. The authors thank Siyu Chen, Ziyue Chen and Jiarui Yu, undergraduate students from Zhejiang University, for their assistance in the experiment.

CRediT

S. Da: Writing - Original Draft, Methodology, Conceptualization, Formal analysis, Investigation; H. Haonan: Writing - Review & Editing; L. Ning: Formal analysis, Methodology, Conceptualization, Writing - Review & Editing; L. Yiwei: Writing - Review & Editing; C. Demartino: Supervision, Writing - Review & Editing.

Declaration of Competing Interest

The authors declare that they have no known competing financial interests or personal relationships that could have appeared to influence the work reported in this paper.

Data availability

The data that support the findings of this study are available from the corresponding author, S.D., upon reasonable request.

References

[1] S. R. Imadi, I. Mahmood, A. G. Kazi, Bamboo fiber processing, properties, and applications, in: Biomass and bioenergy, Springer, 2014, pp. 27–46.

[2] Y. Xiao, Z. Li, K. Liu, Modern Engineered Bamboo Structures: Proceedings of the Third International Conference on Modern Bamboo Structures (ICBS 2018), June 25-27, 2018, Beijing, China, CRC Press, 2019.

[3] J. Zhou, Y. H. Chui, M. Gong, L. Hu, Elastic properties of full-size mass timber panels: Characterization using modal testing and comparison with model predictions, Composites Part B: Engineering 112 (2017) 203–212.

[4] P. Wei, B. J. Wang, H. Li, L. Wang, S. Peng, L. Zhang, A comparative study of compression behaviors of cross-laminated timber and glued-laminated timber columns, Construction and Building Materials 222 (2019) 86–95.

[5] H.-t. Li, Q.-s. Zhang, D.-s. Huang, A. J. Deeks, Compressive performance of laminated bamboo, Composites Part B: Engineering 54 (2013) 319–328.

[6] D. Huang, Y. Bian, A. Zhou, B. Sheng, Experimental study on stress–strain relationships and failure mechanisms of parallel strand bamboo made from phyllostachys, Construction and Building Materials 77 (2015) 130–138.

[7] Y. Wei, S. Tang, X. Ji, K. Zhao, G. Li, Stress-strain behavior and model of bamboo scrimber under cyclic axial compression, Engineering Structures 209 (2020) 110279.

[8] Y. Xiao, Q. Zhou, B. Shan, Design and construction of modern bamboo bridges, Journal of Bridge Engineering 15 (2010).

[9] A. Bouchaïr, P. Racher, J. Bocquet, Analysis of dowelled timber to timber moment-resisting joints, Materials and Structures 40 (2007) 1127–1141.

[10] Z. Guan, P. Rodd, Hollow steel dowels—a new application in semi-rigid timber connections, Engineering Structures 23 (2001) 110–119.

[11] K. F. Chung, W. Yu, Mechanical properties of structural bamboo for bamboo scaffoldings, Engineering structures 24 (2002) 429–442.

[12] L. Villegas, R. Morán, J. J. García, A new joint to assemble light structures of bamboo slats, Construction and Building Materials 98 (2015) 61–68.

[13] J. J. Janssen, Designing and building with bamboo, International Network for Bamboo and Rattan Netherlands, 2000.

[14] T. Ling, S. Mohrmann, H. Li, N. Bao, M. Gaff, R. Lorenzo, Review on research progress of metal-plate-connected wood joints, Journal of Building Engineering 59 (2022) 105056.

[15] S. Platt, K. Harries, Strength of bolted bamboo laminate connections, in: Proceedings 15th International Conference Non-conventional Materials and Technologies (NOCMAT 15), 2015.

[16] M. He, J. Luo, D. Tao, Z. Li, Y. Sun, G. He, Rotational behavior of bolted glulam beam-to-column connections with knee brace, Engineering Structures 207 (2020) 110251.

[17] F. Lam, M. Gehloff, M. Closen, Moment-resisting bolted timber connections, Proceedings of the Institution of Civil Engineers-Structures and Buildings 163 (2010) 267–274.

[18] Z. Shu, Z. Li, X. Yu, J. Zhang, M. He, Rotational performance of glulam bolted joints: Experimental investigation and analytical approach, Construction and Building Materials 213 (2019) 675–695.

[19] M. Wang, X. Song, X. Gu, J. Tang, Bolted glulam beam-column connections under different combinations of shear and bending, Engineering Structures 181 (2019) 281–292.

[20] Y. Leng, Q. Xu, K. A. Harries, L. Chen, K. Liu, X. Chen, Experimental study on mechanical properties of laminated bamboo beam-to-column connections, Engineering Structures 210 (2020) 110305.

[21] Y. Leng, Z. Wang, M. Xu, Experimental study and analysis on rotational behavior of bamboo scrimber beam-to-column bolted connections, Journal of Structural Engineering 147 (2021) 04021122.

[22] L. Stehn, K. Börjes, The influence of nail ductility on the load capacity of a glulam truss structure, Engineering Structures 26 (2004) 809–816.

[23] P. Kobel, A. Frangi, R. Steiger, Timber trusses made of european beech lvl, in: World Conference on Timber Engineering. Aug, 2016, pp. 22–25.

[24] Z. Shu, B. Ning, J. Chen, Z. Li, M. He, J. Luo, H. Dong, Reinforced moment resisting glulam bolted connection with coupled long steel rod with screwheads for modern timber frame structures, Earthquake Engineering and Structural Dynamics 52 (2022) 845 – 864.

[25] Y. Wu, Y. Xiao, Steel and glubam hybrid space truss, Engineering Structures 171 (2018) 140–153.

[26] A. Tabiei, J. Wu, Three-dimensional nonlinear orthotropic finite element material model for wood, Composite structures 50 (2000) 143–149.

[27] Z. Guan, E. Zhu, Finite element modelling of anisotropic elasto-plastic timber composite beams with openings, Engineering Structures 31 (2009) 394–403.

[28] P. Racher, K. Laplanche, D. Dhima, A. Bouchaïr, Thermo-mechanical analysis of the fire performance of dowelled timber connection, Engineering Structures 32 (2010) 1148–1157.

[29] M. Audebert, D. Dhima, M. Taazount, A. Bouchaïr, Numerical investigations on the thermo-mechanical behavior of steel-to-timber joints exposed to fire, Engineering Structures 33 (2011) 3257–3268.

[30] N. Kharouf, G. McClure, I. Smith, Elasto-plastic modeling of wood bolted connections, Computers & structures 81 (2003) 747–754.

[31] M. Wang, X. Song, X. Gu, Three-dimensional combined elastic-plastic and damage model for nonlinear analysis of wood, J. Struct. Eng 144 (2018) 04018103.

[32] J.-P. Hong, D. Barrett, Three-dimensional finite-element modeling of nailed connections in wood, Journal of Structural Engineering 136 (2010) 715–722.

[33] P. J. Gustafsson, Mean stress approach and initial crack approach, Fracture mechanics models for analysis of timber beams with a hole or a notch—a report of RILEM TC-133. Report TVSM-7134, Lund University, Sweden (2002).
[34] J. Zhang, M. He, Z. Li, Mechanical performance assessment of bolted glulam joints with local cracks, Journal of Materials in Civil Engineering 30 (2018) 04018094.
[35] Z. Zhang, J. Su, Mechanical model of stiffness and load-displacement relationship of timber bolted connections with slotted steel plate, Journal of Tongji University 49 (2021) 312–321.
[36] J. Porteous, A. Kermani, Structural timber design to Eurocode 5, John Wiley & Sons, 2013.
[37] Y. Xiao, Y. Wu, J. Li, R. Yang, An experimental study on shear strength of glubam, Construction and Building Materials 150 (2017) 490–500.
[38] Z. Li, X. He, Z. Cai, R. Wang, Y. Xiao, Mechanical properties of engineered bamboo boards for glubam structures, Journal of Materials in Civil Engineering 33 (2021) 04021058.
[39] D. Shi, C. Demartino, Z. Li, Y. Xiao, Axial load–deformation behavior and fracture characteristics of bolted steel to laminated timber and glubam connections, Composite Structures 305 (2023) 116486.
[40] GB/T50329-2002, Standard for testing methods of timber structures, 2002.
[41] ASTM, Astm d143–09:standard specification for general requirements for wire rods and coarse round wire, carbon steel, and alloy steel, 2009.
[42] ASTM, Astm d5764–97a (2013) standard test method forevaluating dowel-bearing strength of wood and wood-based products, 2013.
[43] D. S. Pilon, A. Palermo, F. Sarti, A. Salenikovich, Benefits of multiple rocking segments for clt and lvl pres-lam wall systems, Soil Dynamics and Earthquake Engineering 117 (2019) 234–244.
[44] L. Boccadoro, S. Zweidler, R. Steiger, A. Frangi, Bending tests on timber-concrete composite members made of beech laminated veneer lumber with notched connection, Engineering Structures 132 (2017) 14–28.
[45] R. Jockwer, G. Fink, J. Köhler, Assessment of the failure behaviour and reliability of timber connections with multiple dowel-type fasteners, Engineering Structures 172 (2018) 76–84.
[46] G. Tang, L. Yin, Z. Li, Y. Li, L. You, Structural behaviors of bolted connections using laminated bamboo and steel plates, in: Structures, volume 20, Elsevier, 2019, pp. 324–339.
[47] Z. Li, C. Wang, R. Wang, Application of screw reinforcement in the slotted-in bamboo-steel-bamboo connections, Structures 33 (2021) 4112–4123.
[48] G. G. Beltran, Determination of the embedding strength of plybamboo (2000).
[49] J. Zhou, D. Huang, F. Zhao, Experimental study on dowel-compression strength of parallel bamboo strand lumber, Build. Struct. 45 (2015) 107–110.
[50] G. Tang, L. Yin, Z. Li, Y. Li, L. You, Structural behaviors of bolted connections using laminated bamboo and steel plates, Structures 20 (2019) 324–339.
[51] A. T. Daloglu, C. G. Vallabhan, Values of k for slab on winkler foundation, Journal of Geotechnical and Geoenvironmental Engineering 126 (2000) 463–471.
[52] ASTM, Astm f1575-03: Standard test method for determining bending yield moment of nails, 2008.
[53] GB50005, Code for design of timber structures, 2017.
[54] E. . European Committee for Standardization (CEN), Timber structures-test methods-cyclic testing of joints made withmechanical fasteners, 2001.
[55] J. Cao, H. Xiong, Y. Liu, Experimental study and analytical model of bolted connections under monotonic loading, Construction and Building Materials 270 (2021) 121380.
[56] J. Cao, H. Xiong, J. Chen, A. Huynh, Bayesian parameter identification for empirical model of clt connections, Construction and Building Materials 218 (2019) 254–269.
[57] E. . European Committee for Standardization (CEN), Timber structures - joints made with mechanical fasteners - general principles for the determination of strength and deformation characteristics, 1991.
[58] Y. Verdret, C. Faye, S. Elachachi, L. Le Magorou, P. Garcia, Experimental investigation on stapled and nailed connections in light timber frame walls, Construction and Building Materials 91 (2015) 260–273.
[59] T. Sartori, R. Tomasi, Experimental investigation on sheathing-to-framing connections in wood shear walls, Engineering Structures 56 (2013) 2197–2205.
[60] W. Seim, M. Kramar, T. Pazlar, T. Vogt, Osb and gfb as sheathing materials for timber-framed shear walls: Comparative study of seismic resistance, Journal of Structural Engineering 142 (2016) E4015004.
[61] J. Cabrero, M. Yurrita, Performance assessment of existing models to predict brittle failure modes of steel-to-timber connections loaded parallel-to-grain with dowel-type fasteners, Engineering Structures 171 (2018) 895–910.
[62] M. Yurrita, J. M. Cabrero, New design model for brittle failure in the parallel-to-grain direction of timber connections with large diameter fasteners, Engineering Structures 217 (2020) 110557.
[63] J. Sjödin, E. Serrano, B. Enquist, An experimental and numerical study of the effect of friction in single dowel joints, Holz als Roh-und Werkstoff 66 (2008) 363–372.
[64] J. Sjödin, C.-J. Johansson, Influence of initial moisture induced stresses in multiple steel-to-timber dowel joints, Holz als Roh-und Werkstoff 65 (2007) 71–77.
[65] J. Sjödin, Strength and Moisture Aspects of Steel Timber Dowel Joints in Glulam Structures: An Experimental and Numerical Study, Ph.D. thesis, Växjö University Press, 2008.
[66] G. Chen, H. Jiang, Y.-f. Yu, T. Zhou, J. Wu, X. Li, Experimental analysis of nailed lbl-to-lbl connections loaded parallel to grain, Materials and Structures 53 (2020) 1–13.
[67] R. Ghosh, S. Gupta, A. Dickinson, M. Browne, Experimental validation of finite element models of intact and implanted composite hemipelvises using digital image correlation, Journal of biomechanical engineering 134 (2012).
[68] S. S. Wang L, Lu Z, Study on twelve elastic constant values of betula platyphylla suk wood, Journal of Beijing Forestry University 56 (2003) 2197–2205.
[69] E. Jalilifar, M. Koliou, W. Pang, Experimental and numerical characterization of monotonic and cyclic performance of cross-laminated timber dowel-type connections, Journal of Structural Engineering 147 (2021) 04021102.
[70] J. Jasieńko, T. Nowak, D. Czepižak, Numerical analysis of cfrp-reinforced wooden beams under bending, in: Proceedings of World Conference of Timber Engineering. Riva del Garda: ID/Paper, 851, 2010.
[71] C. Hong, H. Li, Z. Xiong, R. Lorenzo, X. Li, Z. Wang, Axial compressive behavior of laminated bamboo lumber columns with a chamfered section, in: Structures, volume 33, Elsevier, 2021, pp. 678–692.
[72] B.-H. Xu, A. Bouchaïr, P. Racher, Mechanical behavior and modeling of dowelled steel-to-timber moment-resisting connections, Journal of Structural Engineering 141 (2015) 04014165.
[73] R. Hill, A theory of the yielding and plastic flow of anisotropic metals, Proceedings of the Royal Society of London. Series A.

Mathematical and Physical Sciences 193 (1948) 281–297.
[74] B. Xu, A. Bouchaïr, P. Racher, Analytical study and finite element modelling of timber connections with glued-in rods in bending, Construction and Building Materials 34 (2012) 337–345.
[75] B.-H. Xu, A. Bouchaïr, M. Taazount, P. Racher, Numerical 3d finite element modelling and experimental tests of rounded dovetail connection, European journal of environmental and civil engineering 17 (2013) 564–578.
[76] E. Zhu, Z. Guan, P. Rodd, D. Pope, Fe modelling of osb webbed timber i-beams with openings, in: Proceedings of World Conference on Timber Engineering, 2002, 2002.
[77] ASTM2020, Standard specification for general requirements for wire rods and coarse round wire, carbon steel, and alloy steel, 2020.
[78] J. Zhang, M.-J. He, Z. Li, Numerical analysis on tensile performance of bolted glulam joints with initial local cracks, Journal of Wood Science 64 (2018) 364–376.
[79] E. . European Committee for Standardization (CEN), Design of timber structures: General rules and rules for buildings, 1995.
[80] A. Piekarczuk, M. Malesa, M. Kujawinska, K. Malowany, Application of hybrid fem-dic method for assessment of low cost building structures, Experimental Mechanics 52 (2012) 1297–1311.
[81] R. Tiossi, M. A. Vasco, L. Lin, H. J. Conrad, O. L. Bezzon, R. F. Ribeiro, A. S. Fok, Validation of finite element models for strain analysis of implant-supported prostheses using digital image correlation, Dental Materials 29 (2013) 788–796.
[82] A. Dickinson, A. Taylor, H. Ozturk, M. Browne, Experimental validation of a finite element model of the proximal femur using digital image correlation and a composite bone model, Journal of biomechanical engineering 133 (2011).
[83] H. Everitt, S. L. Evans, C. A. Holt, R. Bigsby, I. Khan, Acetabular component deformation under rim loading using digital image correlation and finite element methods, in: Applied Mechanics and Materials, volume 24, Trans Tech Publ, 2010, pp. 275–280.
[84] B. V. Mai, C. H. Pham, G. J. Hancock, G. D. Nguyen, Block shear strength and behaviour of cold-reduced g450 steel bolted connections using dic, Journal of Constructional Steel Research 157 (2019) 151–160.
[85] J. R. Dhanuskar, L. M. Gupta, Experimental investigation of block shear failure in a single angle tension member, International Journal of Steel Structures 20 (2020) 1636–1650.
[86] E. F. Hansson, Analysis of structural failures in timber structures: Typical causes for failure and failure modes, Engineering Structures 33 (2011) 2978–2982.
[87] A. Hanhijärvi, A. Kevarinmäki, Design method against timber failure mechanisms of dowelled steelto-timber connections, in: Proceeding of 40th CIB-W18-Meeting, Bled (SLO), 2007.
[88] M. Yurrita, J. M. Cabrero, P. Quenneville, Brittle failure in the parallel-to-grain direction of multiple shear softwood timber connections with slotted-in steel plates and dowel-type fasteners, Construction and Building Materials 216 (2019) 296–313.
[89] J.-Q. Yang, S. T. Smith, Y.-F. Wu, P. Feng, Strengthening single-bolt timber joints with externally bonded cfrp composites, in: Structures, volume 28, Elsevier, 2020, pp. 2671–2685.
[90] L. Yingyang, S. Jiajia, Mechanical model of stiffness and load displacement relationship of timber bolted connection with slotted steel plate, Journal of Tongji University (2021).
[91] Y. Bai, B. Jiang, L. Yang, Y. Liu, X. Wang, Z. Li, Adoption of size effect combined with winkler elastic foundation beam theory in section shield tunnel under underground space development, Arabian Journal of Geosciences 14 (2021) 1–8.
[92] Z. Zhang, M. Huang, C. Xu, Y. Jiang, W. Wang, Simplified solution for tunnel-soil-pile interaction in pasternak's foundation model, Tunnelling and Underground Space Technology 78 (2018) 146–158.
[93] Y. Liu, Y. Wang, Y. Zhang, M. Chen, X. Nie, Force–displacement relations of bolted timber joints with slotted-in steel plates parallel to the grain, Journal of Wood Science 66 (2020) 1–13.

Appendix A. Loading protocol and definition of performance indeces

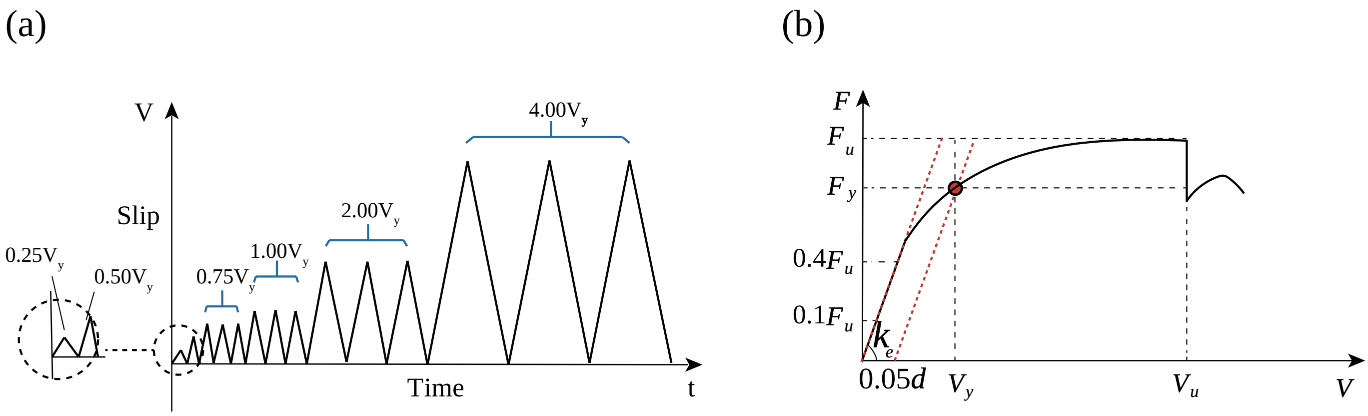

Figure A.23: Loading regime for cyclic testing (a) and definition of k_e, F_y, F_u, and V_u and V_y according to ASTM D5764-97a [42] (b).

Appendix B. Summary of results of tensile monotonic tests

Table B.7: Summary of mechanical indicators (k_e, F_y, F_u, V_y, V_u and D) for all the tests. (Over-bar: average across the tests; CV: Coefficient of variation). After Shi et al. [39].

ID	k_e [kN/mm]	$\bar{k}_e$	CV [%]	F_y [kN]	$\bar{F}_y$	CV [%]	F_u [kN]	$\bar{F}_u$	CV [%]	V_y [mm]	$\bar{V}_y$	CV [%]	V_u [mm]	$\bar{V}_u$	CV [%]	D	$\bar{D}$	CV [%]
LMS8-1	20.95			15.06			21.03			1.31			26.56			26.53		
LMS8-2	16.22	20.29	20.63	12.39	13.19	12.27	23.34	21.19	9.77	0.89	1.09	19.27	27.46	27.21	2.09	18.13	22.05	20.82
LMS8-3	23.73			12.13			19.20			1.08			27.61			21.49		
LMS10-1	30.81			20.10			24.32			1.27			12.05			8.74		
LMS10-2	22.77	24.61	13.84	17.99	19.33	5.40	21.55	22.76	8.38	1.15	1.23	5.69	17.92	15.86	20.81	11.96	9.30	24.23
LMS10-3	20.24			19.91			22.41			1.26			17.60			7.20		
LMD8-1	26.10			23.69			33.48			1.74			9.68			5.53		
LMD8-2	29.76	30.28	14.36	21.73	22.95	4.76	30.38	31.74	4.98	1.12	1.31	28.24	11.03	10.91	10.82	7.80	7.40	32.99
LMD8-3	34.99			23.42			31.38			1.08			12.03			8.88		
LMD10-1	40.70			35.31			36.69			1.45			4.56			2.94		
LMD10-2	44.84	46.22	15.40	36.17	36.97	6.52	43.75	42.54	12.56	1.31	1.36	5.88	6.04	5.00	18.00	2.84	2.98	21.29
LMD10-3	53.13			39.43			47.16			1.31			4.40			3.14		
GMS8-1	28.77			17.06			27.30			1.04			10.43			6.58		
GMS8-2	23.95	24.48	16.48	17.01	17.25	1.98	30.60	30.40	9.87	1.19	1.15	9.57	14.45	13.45	19.78	6.35	7.22	11.32
GMS8-3	20.73			17.68			33.30			1.24			15.46			8.74		
GMS10-1	34.99			27.20			38.59			1.30			9.09			4.80		
GMS10-2	44.54	37.48	16.60	26.50	26.97	1.41	38.46	38.27	1.18	1.10	1.25	11.20	7.75	8.15	10.06	6.14	5.19	13.00
GMS10-3	32.92			27.20			37.76			1.37			7.61			4.64		
GMD8-1	31.71			36.19			45.07			1.61			5.14			2.10		
GMD8-2	39.34	33.33	18.78	34.52	36.47	3.38	42.12	43.21	3.75	1.36	1.41	12.06	3.87	3.89	31.88	2.39	1.93	21.03
GMD8-3	28.92			38.70			42.43			1.28			2.66			1.31		
GMD10-1	58.86			53.30			60.25			1.48			4.50			3.04		
GMD10-2	43.92	49.70	15.89	53.97	54.03	1.22	62.98	62.15	2.65	1.80	1.69	10.65	3.99	4.23	6.15	2.22	1.98	17.79
GMD10-3	46.33			54.83			63.21			1.80			4.20			2.34		

Appendix C. Failure modes and bolt deformation after test for typical specimen in each group

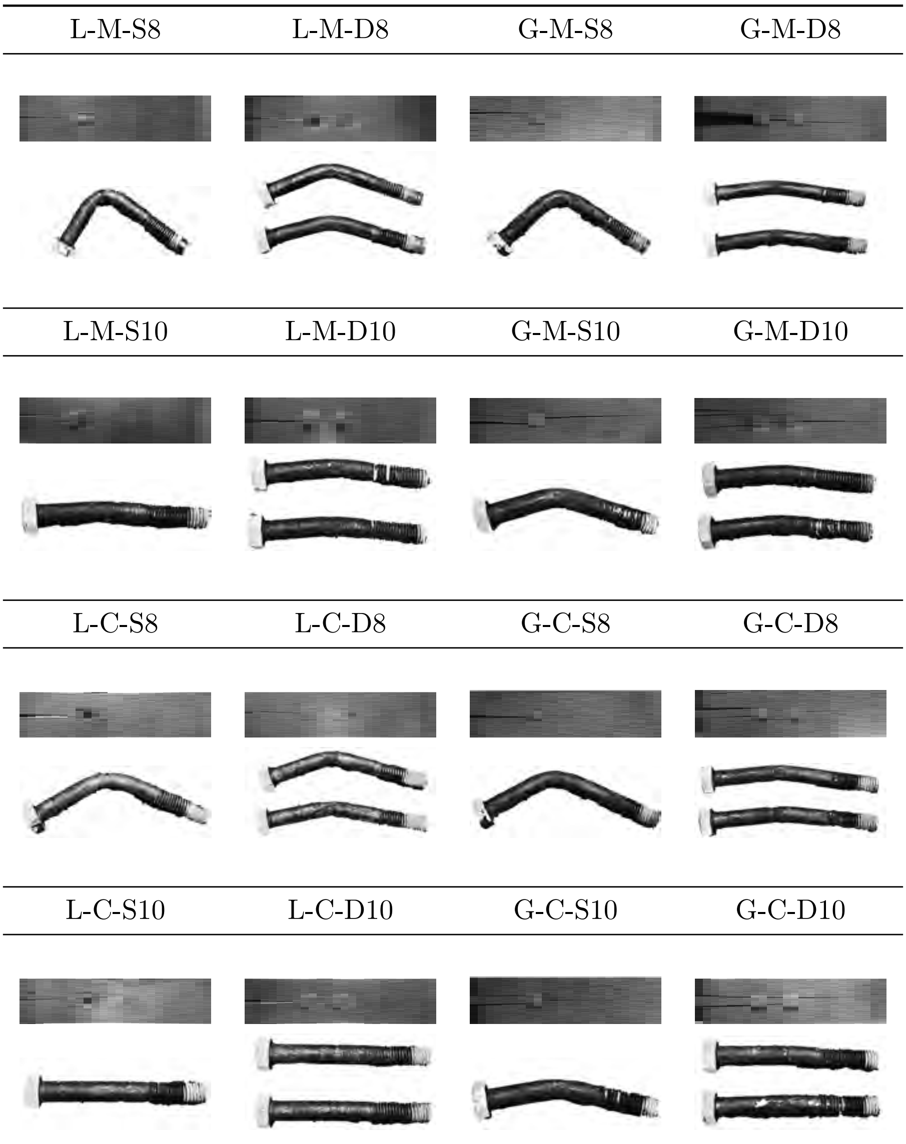

Figure C.24: Failure pattern and bolt deformation after the test. The first two columns show the crack pattern for LVL specimen and the last two columns show glubam specimen. The first two rows show the monotonic cases and the last two rows show the cyclic cases.

Appendix D. Comparison of the tested results, FEM results, and predicted results by EC5 under monotonic loading

Table D.8: Comparison of initial stiffness and maximum load between test and predicted value by FEM and EC5 [79]. The error is calculated as the difference between the considered variable and $k_{e.Test}$ ($F_{u.Test}$,D_{Test}) normalized by $k_{e.Test}$ ($F_{u.Test}$,D_{Test}). $k_{e.Test}$ is the average elastic stiffness measured from the tests (see Table B.7). $k_{e.FEM}$ is the elastic stiffness determined from the FE analyses. $k_{e.EC5}$ is the elastic stiffness calculated according to EC5. $F_{u.Test}$ is the average maximum load measured from the tests (see Table B.7). $F_{u.FEM}$ is the maximum load determined from the FE analyses. $F_{u.EC5}$ is the maximum load calculated according to EC5. D_{Test} is the average ductility obtained from the tests (see Table B.7). D_{FEM} is the ductility determined from the FE analyses.

Conf.	Units	L-MS8		L-MS10		G-MS8		G-MS10		L-MD8		L-MD10		G-MD8		G-MD10	
		value	error	value	error	value	error	value	error	value	error	value	error	value	error	value	error
$k_{e.Test}$	kN/mm	20.29	—	24.61	—	24.48	—	37.48	—	30.28	—	46.22	—	33.33	—	49.70	—
$k_{e.FEM}$	kN/mm	17.76	-12%	26.52	8%	26.24	7%	36.33	-3%	28.89	-5%	51.36	11%	32.53	-2%	47.54	-4%
$k_{e.EC5}$	kN/mm	21.16	4%	26.44	7%	28.52	17%	35.64	-5%	42.32	40%	52.88	14%	57.04	71%	71.28	43%
$F_{u.Test}$	kN	21.19	4%—	22.76	-8%—	30.40	24%—	38.27	2%—	31.74	5%—	42.54	-8%—	43.21	30%—	62.15	25%—
$F_{u.FEM}$	kN	20.33	0.2%	24.38	-1%	30.62	25%	38.71	3%	30.82	2%	49.31	7%	42.51	28%	67.6	36%
$F_{u.EC5}$	kN	16.77	-17%	22.36	-9%	23.31	-5%	35.98	-4%	24.82	-18%	31.08	33%	33.10	-1%	50.00	1%
D_{Test}	—	22.05	—	9.30	—	7.22	—	5.19	—	7.40	—	2.98	—	1.93	—	1.98	—
D_{Fem}	—	21.79	-1%	11.49	24%	11.07	53%	7.10	37%	7.31	-1%	5.24	76%	2.12	9.8%	5.48	177%

792